Comparison of commonly-used microwave radiative transfer models for snow remote sensing

Alain Royer[a,b], Alexandre Roy[a,b], Benoit Montpetit[a*], Olivier Saint-Jean-Rondeau[a,b], Ghislain Picard[c], Ludovic Brucker[d,e] and Alexandre Langlois[a,b]

[a] Centre d'Applications et de Recherches en Télédétection (CARTEL), Université de Sherbrooke, 2500 boul. Université, Sherbrooke, QC, Canada, J1K 2R1.

[b] Centre d'Études Nordiques, Québec, Canada

[c] Université Grenoble Alpes - CNRS, LGGE UMR5183, 38041 Grenoble, France

[d] NASA Goddard Space Flight Center, Cryospheric Sciences Laboratory, Code 615, Greenbelt, MD 20771, USA

[e] Universities Space Research Association, Goddard Earth Sciences Technology and Research, Columbia, MD 21046, USA.

* Now at the Canadian Ice Service, Environment and Climate Change Canada, Ottawa.

Abstract

This paper reviews four commonly-used microwave radiative transfer models that take different electromagnetic approaches to simulate snow brightness temperature (T_B): the Dense Media Radiative Transfer – Multi-Layer model (DMRT-ML), the Dense Media Radiative Transfer – Quasi-Crystalline Approximation Mie scattering of Sticky spheres (DMRT-QMS), the Helsinki University of Technology n-Layers model (HUT-nlayers) and the Microwave Emission Model of Layered Snowpacks (MEMLS). Using the same extensively measured physical snowpack properties, we compared the simulated T_B at 11, 19 and 37 GHz from these four models. The analysis focuses on the impact of using different types of measured snow microstructure metrics in the simulations. In addition to density, snow microstructure is defined for each snow layer by

grain optical diameter (Do) and stickiness for DMRT-ML and DMRT-QMS, mean grain geometrical maximum extent (D_{max}) for HUT n-layers and the exponential correlation length for MEMLS. These metrics were derived from either in-situ measurements of snow specific surface area (SSA) or macrophotos of grain sizes (D_{max}), assuming non-sticky spheres for the DMRT models. Simulated T_B sensitivity analysis using the same inputs shows relatively consistent T_B behavior as a function of Do and density variations for the vertical polarization (maximum deviation of 18 K and 27 K, respectively), while some divergences appear in simulated variations for the polarization ratio (PR). Comparisons with ground-based radiometric measurements show that the simulations based on snow SSA measurements have to be scaled with a model-specific factor of Do in order to minimize the root mean square error (RMSE) between measured and simulated T_B. Results using in-situ grain size measurements (SSA or D_{max}, depending on the model) give a mean T_B RMSE (19 and 37 GHz) of the order of 16-26 K, which is similar for all models when the snow microstructure metrics are scaled. However, the MEMLS model converges to better results when driven by the correlation length estimated from in-situ SSA measurements rather than D_{max} measurements. On a practical level, this paper shows that the SSA parameter, a snow property that is easy to retrieve in-situ, appears to be the most relevant parameter for characterizing snow microstructure, despite the need for a scaling factor.

Keywords: Snow microwave-emission model; Snow microstructure; Radiative transfer model; Canada; Ground-based measurements; Brightness temperature

1. Introduction

In snow remote sensing, a better parameterization of the radiative transfer models (RTM) for simulating snow microwave emission improves our ability to retrieve snowpack characteristics from space-borne observations. Snow microstructure metrics are the main input parameter of the microwave RTM (e.g. Rutter et al., 2009) and its characterization can strongly impact the retrievals from microwave emission measurements for snow monitoring (e.g. Mätzler, 1994; Armstrong and Brodzik, 2002; Kelly et al., 2003; Mätzler et al., 2006; Löwe and Picard, 2015). Thus, given that the available models that are well-defined in the literature and commonly used for snow remote sensing are defined by different snow microstructure parameterizations, a review appears essential. We consider here the following four models: the Dense Media Radiative Transfer– Multi layers (DMRT-ML) model (Picard et al., 2013), the Dense Radiative Transfer Model – Quasi-Crystalline Approximation (QCA) Mie scattering of Sticky spheres (DMRT-QMS) model (Chang et al., 2014), the multi-layer Helsinki University of Technology model (HUT-nlayers) (Lemmetyinen et al., 2010a), and the Microwave Emission Model of Layered Snowpacks (MEMLS) (Proksch et al., 2016; Wiesmann and Mätzler, 1999; Mätzler and Wiesmann, 1999). Several aspects of these models are based on different electromagnetic theories or semi-empirical approaches (multiple scattering and absorption coefficient computations, for example), and they are often driven by sets of different measured inputs for snow grain metrics, such as snow specific surface area (SSA), correlation length or snow grain geometrical extent obtained from visual analysis.

Tedesco and Kim (2006) compared earlier simplified single-layer versions of the DMRT, HUT and MEMLS models based on the snow grain metric given by visual inspection (average size over the snowpack depth of representative small, medium, and large grains in each layer measured using a microscope). MEMLS and HUT-nlayers were compared by Lemmetyinen et al. (2010b) and Pan et al. (2016). DMRT theory and IBA were also recently compared and analyzed (Löwe and Picard, 2015), while Roy et al. (2013) compared DMRT-ML and HUT-nlayers.

Sandells et al. (2016) compared DMRT-ML, HUT-nlayers and MEMLS models considering only the optical diameter generated by snow models. But the four multi-layer models considered were never compared together using coincident sets of measured snow properties. The main challenge in comparing these RTM models is that the input snow microstructure parameters differ in each model and are in some cases difficult or impossible to measure in the field. Three different snow microstructure representations are considered in these models: optical diameter (D_o) and stickiness for DMRT-ML and -QMS, correlation length (p_c) for MEMLS and maximum geometrical extent (D_{max}) for HUT-nlayers. Consequently, some hypotheses are needed for their estimation allowing coherent intercomparison of models (Löwe and Picard, 2015). For example, it was previously shown that the optical diameter derived from the SSA needs to be scaled by a factor in order to be in agreement with measurements when considering DMRT-ML with non-sticky medium (Brucker et al. 2011; Roy et al., 2013; Montpetit et al., 2013; Picard et al. 2014; Dupont et al., 2014). As the physical aspects of each model had already been extensively analyzed, we put the emphasis in this paper on comparing the models with surface-based measured brightness temperature (T_B). The objective is to compare the simulations using the same in-situ measurements of improved snow parameterization, which had never been done.

This paper briefly recalls the main basic fundamentals of these four models and more specifically the different grain size definitions involved (Section 2). After presenting datasets and snow microstructure measurement methods (Section 3), we first compare the four models using a synthetic snowpack to perform a sensitivity analysis (Section 4.1), and we then compare the simulated T_B using sets of measured snow properties against measurements of surface-based radiometric T_B at 11, 19 and 37 GHz (Section 4.3).

2. Models and their respective snow microstructure metric

A synthesis matrix of the four models considered in this study is presented in Table 1. These models are all publicly available (thus specific details of their implementations can be known)

and are extensively described in the references given in Table 1. Readers are invited to consult these references for detailed descriptions of the models, which are based on conceptually different approaches for computing snow electromagnetic properties and radiation transfer in the multi-layers of the snowpack. In this paper, all the simulations were performed using the recommended configuration for DMRT-ML and -QMS, the Improved Born Approximation (IBA) (option 12) for MEMLS and the original version of the extinction coefficient in HUT (see Table 1).

One of the main difficulties in snow radiative transfer is the parameterization of snow microstructure consisting of a high density of scatterers per unit of volume. DMRT-ML and –QMS consider the snow as a collection of sticky spherical ice particles defined by their radius and stickiness (Tsang and Kong, 2001; Tsang et al., 2007), while MEMLS parameterizes snow microstructural properties by a second order statistical function, the two-point correlation function, giving the mutual relationships between two scatterers within a given volume, such as the autocorrelation function (the exponential correlation length p_{ex} is generally used, see Section 2.2 below). HUT is based on empirical scattering and extinction coefficients fitted with the observed maximum dimension of snow grains (D_{max}), or more recently an effective grain size radius (Kontu and Pulliainen, 2010). When using in-situ ground-based measurements of snow microstructure parameterization, practical comparison of these models requires hypotheses to retrieve and link the different metrics. The metrics used in this study are briefly defined below.

Table 1 Comparison between basics of DMRT-ML/-QMS, MEMLS and HUT-nlayers models.

See the Table at the end of the paper.

2.1 DMRT snow microstructure metric

DMRT-ML considers snow grains as spherical particles of ice defined by their radius. Their position (clustering) is controlled by stickiness. For snow having a wide range of grain shape, the radius of equivalent spheres can be objectively defined by their optical radius (Ro), which can

always be derived from the SSA via the optical equivalent radius. The snow SSA is the surface of the air/snow interface (S) per unit of mass: $M=\rho_{snow}$•Volume: SSA=S/M = S/(ρ_{ice}•Volume) in m^2 kg^{-1}, where ρ_{ice} is the ice density (917 kg m^{-3}). SSA measurements are described in Section 3. For spheres or snow assimilated as sphere equivalent (see the review paper by Domine et al., 2008), the optical radius (Ro) is expressed as (Ro in mm, ρ_{ice} in kg m^{-3} and SSA in m^2 kg^{-1}):

$$Ro = 3.10^3/(\rho_{ice}\bullet SSA) \quad (1).$$

Since any measurements can be used to estimate stickiness, Brucker et al. (2011), Roy et al. (2013), Dupont et al. (2014) and Picard et al. (2014), considering a non-sticky medium, have shown that Ro should be multiplied by the scaling factor ϕ_{DMRT} when Ro is derived from SSA measurements (R'o in mm):

$$R'o = \phi_{DMRT}Ro = 3.10^3\,\phi_{DMRT}/(\rho_{ice}\bullet SSA) \quad (2).$$

This scaling factor is discussed in Section 4.2. Roy et al. (2013) also showed that the following relationship (inspired by Kontu and Pulliainen, 2010) can be used for an effective optical radius of snow grains derived from SSA measurements:

$$R''o\ [mm] = 1.1\ [1 - \exp(-24.6.10^3/(\rho_{ice}\bullet SSA)] \quad (3).$$

The stickiness parameter (τ), used by DMRT theory (Tsang and Kong, 2001), is inversely proportional to the contact adhesion between spheres. It can be linked to the cohesion or to a degree of connectivity between grains. Thus, for non-sticky spheres: $\tau = \infty$; for snow with clusters (aggregates) or grains with high strength of adhesion, τ decreases (for example τ = 1 to 0.2 or less). DMRT-ML uses the "short range" approximation (Tsang and Kong, 2001) which implies that grains and aggregates should remain small compared to the wavelength. Roy et al., (2013) hypothesized that the needed scaling factor (ϕ_{DMRT}) is related to the assumption of non-sticky spheres ($\tau = \infty$) and to the assumption of monodisperse grain size distribution. This scaling factor is therefore a surrogate of the stickiness parameter which cannot practically be measured in the field (see Löwe and Picard, 2015).

2.2 MEMLS snow microstructure metric

MEMLS uses the correlation length (p_c) for describing snow microstructure, which is the slope of the spatial autocorrelation function at the origin (i.e. the derivative of this function). This parameter might be derived from micro-computed tomography measurements (micro-CT) (Löwe et al., 2013) or by high-quality stereological method (see Riche et al., 2012), but its rapid derivation from field measurements is still difficult. Recently, Proksch et al. (2015) proposed a relationship between Snow-Micropen measurements and correlation length that has not yet been validated for microwave emission applications.

Here, we first estimate the correlation length from the equivalent sphere grain radius (Ro) as proposed by Mätzler (2002), following the Debye relationship:

$$p_c = 4/3\ Ro\ (1 - \nu) \qquad (4),$$

where ν is the ice volume fraction: $\nu = \rho_{snow}/\rho_{ice}$.

While there is no experimental relationship between simultaneous measurements of p_c (from micro-CT measurements) and SSA measurements, Montpetit et al. (2013) showed that the following relationship gives optimized simulated T_B using MEMLS driven with SSA measurements (p'_c in mm and SSA in $m^2\ kg^{-1}$):

$$p'_c\ [mm] = 4.10^3\ \phi_{MEMLS}\ (1 - \nu)/(\rho_{ice} \bullet SSA) \qquad (5),$$

where ϕ_{MEMLS} is a scaling factor and SSA is measured in-situ.

If the autocorrelation function is approximated (fitted) by an exponential function of the form: $\exp(-x/p_{ex})$, one can derive the exponential correlation length p_{ex}. According to the type of snow, p_{ex} is different from p_c (Krol and Löwe, 2016; Matzler, 2002). For microwave measurements, p_{ex} is generally preferred to p_c, and Mätzler (2002) found in general that $p_{ex} \approx 0.75 p_c$, giving from (1) and (4):

$$p_{ex}\ [mm] \approx Ro\ (1 - \nu) = 3.10^3\ (1 - \nu)/(\rho_{ice} \bullet SSA) \qquad (6).$$

On the other hand, previous studies from Mätzler (1997) have shown that p_c is closer to the minimum characteristic extent of the grain than related to the maximum geometrical particle extent. Mätzler (2002) gives a series of measurements of p_c, p_{ex} and visually estimated grain size D_{max} (defined below) for 20 samples of different snow types showing the correspondence between these parameters. Using these data, p_{ex} (or p_c) can be expressed as a logarithmic function of D_{max}:

$$p_{ex} = a + b \ln(D_{max}) \quad \text{for } \nu > \nu_{th} \text{ and } D_{max} > D_{max,th} \text{ in mm}$$
$$p_{ex} = C^{st} \quad \text{otherwise} \qquad (7),$$

where ν_{th} and $D_{max,th}$ are thresholds delimitating the range of validity of the proposed model, and C^{st} is a constant for values below these thresholds.

Using the Mätzler (2002) data, Durand et al. (2008) found that a = 0.18 and b = 0.09 for $\nu > 0.2$ and $D_{max} > 0.125$ mm , and that $p_{ex} = 0.05 \pm 0.017$ otherwise.

2.3 HUT snow microstructure metric

HUT input is based on individual grain size. There are many ways to describe the geometrical grain size of snow (Colbeck et al., 1990; Lesaffre et al., 1998; Fierz et al., 2009). Among them, one can cite the circle (or ellipsoid) that better encompasses the snow grain; the equivalent radius given by the ratio between projected grain area and its perimeter; the mean convex radius of curvature; or the greatest extent of the prevailing or characteristic grains: D_{max}. The latter corresponds to the maximum dimension of the "intermediate grain size" and has long been a classical parameter routinely used to visually characterize snow structure in the field (see Colbeck et al., 1990; Fierz et al., 2009). The HUT model can be driven either directly by D_{max}, or by an effective grain diameter ($D_{max,eff}$) derived from D_{max} following the relationship that minimized the differences between measured and simulated T_B, as proposed by Kontu and Pulliainen (2010) (see also Lemmetyinen et al., 2010a and 2015; Pan et al., 2016):

$$D_{max,eff} = 1.5\ (1 - \exp(-1.5\ D_{max})) \quad (8),$$

where $D_{max,eff}$ and D_{max} are in mm.

However, in this study, it appears that this relationship (Eq. 8) for estimating the $D_{max,eff}$ does not give a good agreement, due to the lack of convergence in the optimization. This results from the large digitized D_{max} measurement values obtained in this study (see Section 4.2), and Eq. 8 leads to a unique $D_{max,eff}$. In the model comparison (Section 4.3), we thus consider $D_{max,eff} = 0.5\ D_{max}$, derived from an optimization that reduces the difference between simulated and measured T_B (method of Roy et al., 2013).

When SSA is measured, Roy et al. (2013) use Equation (2), with a different scaling factor (ϕ_{HUT}) relative to the effective grain size in HUT simulations:

$$Do_{eff}\ [mm] = 6.10^3\ \phi_{HUT}/(\rho_{ice} \bullet SSA) \quad (9).$$

All the ϕ factors (ϕ_{DMRT}, ϕ_{MEMLS} and ϕ_{HUT}) are further discussed in the results section. Field measurement methods for SSA and D_{max} estimates are presented in Section 3.

2.4 Scaling factors for the models driven by SSA measurements

The scaling factor ϕ depends upon the model considered and the type of snow. The change in this scaling factor is linked to other microstructure parameters such as stickiness and to the fact that we assume a monodisperse size distribution of snow grain (see the discussions in Brucker et al., 2011; Roy et al., 2013 and Löwe and Picard, 2015). It cannot be explained by measurement uncertainties (Roy et al., 2016). Löwe and Picard (2015) theoretically demonstrate the need of grain size scaling between the optical diameter and the equivalent sticky hard sphere diameter. For DMRT-ML with the assumption of non-sticky spheres, the ϕ factor obtained varies from 2.3 to 3.5 depending on the type of snow (Table 2). The amplitude of this factor may also partly be affected by errors in snow measurements and possibly in the soil parameters. Precise explanation

of these differences in the ϕ factor needs further study but is outside the scope of this paper. Here we used ϕ = 3.3, 1.3 and 3.7, respectively for DMRT-ML, MEMLS and HUT-nlayers (Table 2) in order to compare the known optimized models when driven by SSA measurements compared to simulations driven by D_{max} measurements.

Table 2. Scaling factor ϕ to be applied on the snow microstructure metric derived from in-situ SSA measurements, as a function of the RTM considered and the type of snow. All SSA measurements were derived from the DUFISSS's type approach (see Section 3.1), except *: the values depend upon the method used for retrieving SSA; and **: SSA retrieved from ASSAP device (see details in the given references, last column).

Radiative Transfer Models	Snow μstructure Metrics	Sites	ϕ	References
MEMLS	$p'_c=4.10^3\ \phi\ (1-\nu)/(\rho_{ice}\cdot SSA)$ Eq. 5	Canada: Arctic, Subarctic, South Québec	**1.3**	Montpetit et al., 2013
DMRT-ML (no stickiness)	$R'o=3.10^3\phi/(\rho_{ice}\cdot SSA)$ Eq. 2	Dome C Antarctica	**1.89, 2.5, 2.85***	Brucker et al., 2011
		Dome C Antarctica	**2.3****	Picard et al., 2014
		Barnes Ice Cap Canada Arctic	**3.5**	Dupont et al., 2014
		Canada: Arctic, Subarctic, South Québec	**3.3**	Roy et al., 2013
HUT-nlayers	$Ro_{eff}=3.10^3\phi/(\rho_{ice}\cdot SSA)$ Eq. 9	Canada: Arctic, Subarctic, South Québec	**3.7**	Roy et al., 2013

2.5 Radiative Transfer Model inputs

Apart from the snow microstructure parameterization, all other input parameters required by the four models are the same for each layer defined by its thickness, snow temperature and density. Here, we only considered dry snow. An important contribution to snowpack emission can emanate from the soil under the snowpack, in particular at low frequencies. For the intercomparison in this study, we thus used the same rough soil reflectivity model proposed by Wegmüller and Mätzler (1999) (see the review of Montpetit et al., 2015a). At a given frequency, the soil parameterization is defined by the soil/snow interface reflectivity in horizontal polarization (Γ_H) and vertical polarization (Γ_V) with the following equations for an incidence angle (θ) lower than 60°:

$$\Gamma_H = \Gamma_H^{Fresnel} exp\left(-(k\sigma)^{\sqrt{-0.1cos\theta}}\right) \quad (10),$$

$$\Gamma_V = \Gamma_H cos\theta^{\beta}$$

where k is the incident medium wave number (air or snow), $\Gamma_H^{Fresnel}$ is the Fresnel reflectivity function which depends on the soil permittivity (ε_{soil}), σ is the soil roughness parameter and β is a scaling factor for deriving the reflectivity at vertical polarization from the computed reflectivity at horizontal polarization. Following Montpetit et al. (2015b), we consider the optimized values of ε_{soil}^{eff}, σ^{eff} and β^{eff} parameters for each frequency given in Table 3.

Table 3. Soil parameters considered for the three models (see Eq. 10).

Frequency (GHz)	ε_{soil}^{eff},	β^{eff}	σ^{eff} (cm)
11	3.18-0.006134j	1.08	0.19
19	3.42-0.00508j	0.72	
37	4.47-0.32643j	0.42	

For comparisons between simulated T_B and measurements, the downwelling sky radiance reflected by the snowpack toward the radiometer has to be taken into account (Montpetit et al.,

2013; Courtemanche et al., 2015; Roy et al., 2016). In each surface-based radiometric measurement, the atmospheric contribution was calculated using the atmospheric Millimeter-wave Propagation Model (MPM: Liebe, 1989) implemented in the HUT snow emission model (Pulliainen et al., 1999). The atmospheric model was driven with the air temperature and precipitable water of the atmospheric layers above the surface given by the 29 atmospheric layers of the North American Regional Reanalysis (NARR) (Mesinger et al., 2006) for the NARR pixel and time of measurements. Note that all the snowpits were located in open areas where no vegetation could contribute to the measured T_B (see the discussion in Roy et al., 2016). We previously validated this procedure against sky microwave measurements (see Courtemanche et al., 2015).

3. Ground-based measurement dataset

3.1 Optical radius retrieved from SSA measurements using IRIS

A light short-wave infrared laser-based system measuring snow albedo through an integrating sphere (InfraRed Integrating Sphere, IRIS), similar to the system previously proposed by Gallet et al. (2009), was used for SSA measurements (Montpetit et al., 2012). Relatively good accuracy (12-15%) and reproducibility in SSA measurements are obtained using the IRIS system on extracted samples. Gallet et al. (2009) and Montpetit et al. (2012) describe in detail these devices (Dual Frequency Integrating Sphere for Snow SSA: DUFISSS and IRIS, respectively). Lambertian targets with known reflectance values (Spectralon: 0.06, 0.25 0.60, 0.79, and 0.98 at 1.33 μm) were used to calibrate the device before and after each series of measurements at each site. From the reflectance, the SSA was calculated as described by Montpetit et al. (2012). SSA measurements allow us to estimate the mean optical radius of grain sizes of each layer (Eq.1), assuming that all grains have the same size (monodisperse size distribution).

3.2 D_{max} measurements using multidirectional lighting macrophotos in the Shadow-box

Macrophotos of snow grain samples have been widely used in numerous studies (e.g. Colbeck, 1990; Fierz et al., 2009). In order to improve geometrical snow grain parameterization, we developed an optical system that uses, within an enclosed box (30x30x30 cm), five light-emitting diodes that provide five-direction (nadir, N, E, S and W) illumination of a gridded plate upon which snow grains are placed (Fig. 1). Five photographs are taken successively for each illuminated direction with a Nikon D40 fitted with a macro lens (Fig. 1). The projected area of the grain is extracted from a first photograph with the diode illuminating from nadir and the four other photographs allow the digitization of the projected shadows. Knowing the angles of illumination and the exact position of each grain on the gridded illuminated plate, it is possible to calculate the height of the grain envelope using the tangent illumination path corresponding to the projected shadow in each direction. We thus derived a numerical height model of each snow grain and reconstructed a 3D representation of the snow grain envelope (Fig. 1). From this elevation model, one can derive multiple size parameters: D_{max}, minor and major axis of the envelope ellipsoid, projected area, mean height, maximum height and apparent volume and surface area. All of these parameters are then averaged for each sample. This device (called *Shadow-box*) is very easy to handle in the field, and improves the retrieval of a 3D representation of the snow grains. It is also useful to characterize snow grain shapes and types of extracted snow samples. Using calibrated spheres (steel balls from 0.8 to 4.8 mm), the retrieval error (bias) on D_{max} was estimated of the order of 0.03 mm. The measurement protocol is as follows: we gently cover the plate with separated grains of a snow sample extracted from each snowpack layer (approximately every 3 cm over the snowpit), and take the five consecutive macrophotos, including identifications of the snowpit and layer. We then systematically manually digitize the contour of all the grains on the plate to estimate the mean D_{max} (2D) values for each snowpack layer. The shadows help to discriminate individual grains in aggregates or when grains are stuck together.

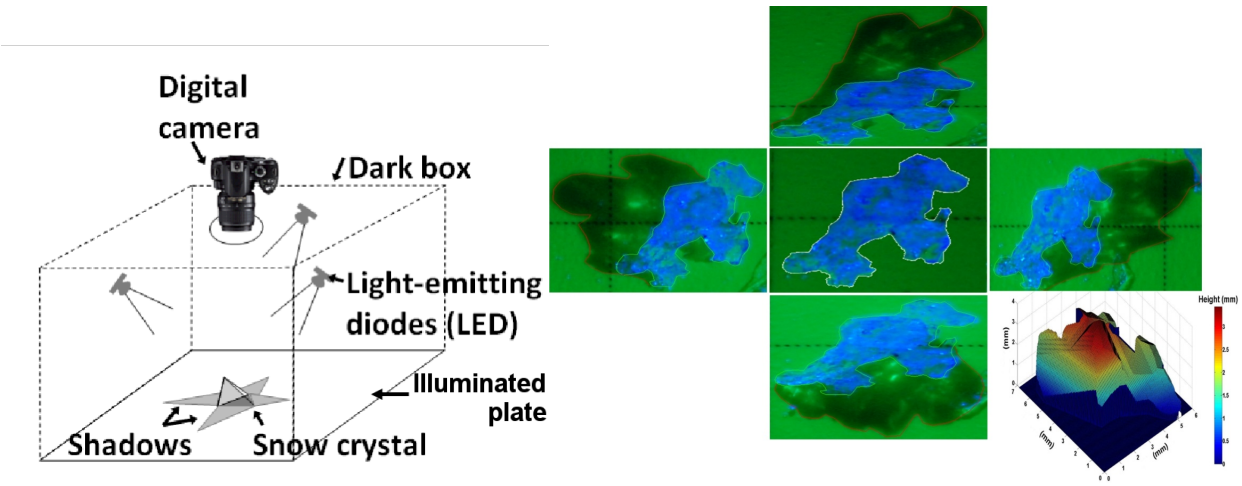

Fig. 1 Shadow-box. Snow grains placed on the plate are successively illuminated from four directions by four LEDs and by one LED from the nadir, producing five macrophotos (right), from which a 3D envelope model of the grain can be retrieved after manual digitization of the shadows. The size of the grain shown is 7 mm.

3.3 Correlation length

Since no direct measurement of correlation length was carried out, the values of correlation length (p_c or p_{ex}) used as inputs for MEMLS were estimated in three ways: (1) from the retrieved optical grain size radius (SSA measurements) and the fractional volume (Debye relationship, Eq. 5) (hereafter labeled MEMLS_Do); (2) from the measured values of mean D_{max} grain size (2D Shadow-box) and fractional volume based on the Mätzler relationship (Durand et al., 2008) (hereafter labeled MEMLS_D_{max_pex}); and (3) from p_{ex} based on the observed linear relationship between p_c and Dmax shown in the results section (see Fig. 5) (hereafter labeled MEMLS_D_{max}_lin).

3.4 T_B measurements

T_B measurements were taken for every snowpit at 10.67 (hereafter noted 11), 19 and 37 GHz in vertical polarization (V-pol) and horizontal polarization (H-pol) at a height of approximately 2 m

above the surface using PR-series field radiometers (Radiometrics Corporation, Boulder, CO, USA) at an incidence angle of 54°-55°, which is close to the measurement incidence angle of the Advanced Microwave Scanning Radiometer – Earth Observing System (AMSR-E) and Special Sensor Microwave Imager (SSM/I) space-based sensors. The ellipsoidal footprint of measurements at the snow surface was approximately 0.5 m × 0.65 m. The radiometer calibration was based on two measurements taken with the absorbing foam Eccosorb© (Cuming Microwave Corporation, MA, USA) at the ambient temperature (i.e. warm reference) and another taken over a surface of liquid nitrogen (i.e. cold reference) (Asmus and Grant, 1999; Langlois, 2015). In the worst case, measurement error for the calibration target was estimated at ±2 K. Ambient and cold point measurements from before and after the field campaign periods (typically separated by five to ten days) were used to produce a final calibrated T_B data set.

3.5 In-situ snow data

The snow data needed by the models were derived from in-situ measurements in three northern Canadian regions. Table 4 provides the data from the Arctic: Churchill (MB), the Subarctic region: James Bay (QC), and southern regions of Québec: Sherbrooke (QC) and St-Romain (QC). All sites were already well-described in the references given in the Table 4. This database of 32 snowpits encompasses a wide range of snow types (i.e. metamorphic processes and stratigraphy), typical of North American environments. For each site, profiles of snow temperature, snow density, and snow microstructure were taken at a vertical resolution of 3 or 5 cm in the footprint of the microwave radiometers. The density was measured with a 185 cm^3 density cutter, and the samples were weighed with a 100 g Pesola light series scale with an accuracy value of 1 g. The temperature was measured with a Traceable 2000 digital temperature probe (±0.1°C). The microstructure of each layer was defined with both SSA (optical radius) and D_{max} measurements, the latter using macrophotos (Shadow-box). In Table 4, we give the vertically averaged values of density, optical radius and D_{max}, weighted by the snow layer

thicknesses and the derived bulk p'_c (from Eq. 5) were also estimated (9th column). The stratigraphy was examined at each site, and all ice lenses (or crusts), when present, were identified and measured. Their density was not measured as this is very difficult to properly sample. All the microwave and snow measurements were always synchronised in time. All these 32 sites (Table 4) were used for model comparison.

Table 4. Summary of the snow parameters of all sites analyzed in this study. Site name: CHxx corresponds to Churchill, MB sites (Roy et al., 2013; Montpetit et al., 2013); SIRSP4 and RoSP1 correspond to the southern Québec sites, respectively to the SIRENE site at Sherbrooke, QC and to the St-Romain, QC site (Roy et al., 2013); BJxx sites corresponds to the James Bay, Nunavik, QC sites (Subarctic sites) (Roy et al., 2016). The snowpits where an ice lens was observed are identified (last column).

	Site Name	Snow depth (m)	Tsnow (K)	Density (kg/m^3)	Tsoil (K)	Optical radius (mm)	Dmax (mm)	Bulk p'_c (Eq. 5)	Ice lens
1	CH42	0.37	259.4	289.4	267.9	0.22	4.43	0.267	
2	CH43	0.70	257.3	311.4	270.3	0.20	2.68	0.231	
3	CH83	1.18	269.4	372.6	272.7	0.19	2.83	0.199	
4	CH90	0.82	265.3	284.0	271.8	0.18	3.43	0.213	
5	CH91	0.91	267.1	324.7	272.5	0.19	4.16	0.210	
6	CH92	0.83	268.3	292.8	272.9	0.22	3.10	0.262	
7	CH95	1.74	266.0	380.3	272.8	0.15	1.89	0.150	
8	CH96	1.80	266.8	367.8	272.9	0.17	2.20	0.172	
9	CH97	1.50	266.4	380.9	272.7	0.18	2.07	0.178	
10	CH98	1.19	265.8	351.4	272.5	0.16	2.04	0.166	
11	CH104	0.48	255.2	261.4	269.6	0.32	4.90	0.393	
12	CH105	0.45	258.7	229.7	270.3	0.32	6.11	0.419	
13	CH111	0.44	252.5	284.6	269.8	0.25	4.54	0.303	
14	CH55	0.51	258.5	308.4	269.7	0.19	3.54	0.214	
15	CH56	0.35	254.9	314.6	267.2	0.20	3.15	0.231	
16	CH99	0.57	259.3	328.0	270.1	0.23	4.02	0.255	
17	CH101	0.19	259.1	263.2	264.6	0.33	4.88	0.403	
18	CH54	0.48	257.1	345.0	269.5	0.20	4.51	0.215	x
19	CH57	0.25	260.2	321.9	266.1	0.20	3.50	0.224	
20	CH58	0.35	256.5	304.6	267.9	0.16	4.84	0.189	x
21	CH59	0.65	260.2	276.6	271.7	0.23	3.71	0.274	x
22	CH60	0.14	270.4	288.3	262.2	0.27	3.83	0.325	x
23	CH61	1.03	260.5	400.8	272.5	0.19	2.68	0.187	
24	CH82	0.35	266.5	285.4	270.8	0.37	4.08	0.446	
25	CH93	0.82	279.6	311.9	271.9	0.28	4.43	0.325	x

26	CH100	0.43	259.8	295.8	269.2	0.28	4.78	0.328	x
27	CH114	0.72	283.2	323.0	272.8	0.33	3.19	0.373	x
28	CH115	0.31	271.4	313.6	272.2	0.33	5.11	0.382	
29	SIRSP4	0.33	271.5	245.9	273.0	0.14	3.07	0.173	
30	RoSP1	0.47	269.4	179.2	273.5	0.08	1.05	0.107	x
31	BJjan1	0.51	266.8	284.9	271.5	0.16	3.07	0.191	x
32	BJfev2	0.66	265.8	245.1	273.1	0.18	2.01	0.229	x

4. Results

A sensitivity analysis is first performed to compare the four models considered with the same inputs considering a synthetic snowpack (Section 4.1). We then discuss the consistency between the grain size measurements (Section 4.2), and we compare the simulations with ground-based measurements (Section 4.3).

4.1 Sensitivity analysis of the three models

Based on an identical synthetic snowpack, we seek to illustrate model sensitivity to three parameters: - grain size (Fig. 2); - density (Fig. 3); - and ice lens in the snowpack (Fig. 4).

Fig. 2 shows the comparison between the 37 GHz brightness temperature variations as a function of Do, using the four models in a very simple synthetic case defined by one layer of 1 m thickness with a mean uniform density of 250 kg m^{-3}. The incidence angle of T_B simulations is 55°. All input parameters were the same for the four models and the different microstructure metrics were derived from the same initial grain parameter (Do) using equations (2), (5) and (9). To define the optical diameter of each model, we used the scaled factors defined in previous analysis (see discussion in Section 4.2). These factors optimize the simulations compared to in-situ radiometric measurements for real snowpacks. The relationships defining the microstructure metrics were derived from Equations (2), (5) and (9), respectively for DMRT-ML (assuming non-sticky spheres) (Roy at al., 2013), MEMLS-IBA (Montpetit et al., 2013) and HUT (Roy et

al., 2013). For DMRT-QMS, we used the same relationship as for DMRT-ML, and also assuming non-sticky spheres. The comparison in Fig. 2 is thus performed using the following equations:

$$\begin{cases} \text{DMRT-ML/-QMS: } D'o = 3.3\ Do \\ \text{MEMLS: } p'_c = 1.3\ \ (2/3)\ Do\ (1-\nu) \\ \text{HUT: } Do_{eff} = 3.7\ Do \end{cases} \quad (11)$$

The results show that the T_B simulated by the four models similarly decrease with the grain size, as expected due to the high sensitivity of microwave attenuation to grain size at 37 GHz. Using the scaling factors for the input grain size metrics given in Eq. 11, the simulated T_B V-pol are close for Do around 0.5 mm and for Do<0.2 (Fig. 2, top). However, MEMLS T_B values appear underestimated by 18 K compared to DMRT-ML/-QMS around Do = 0.3 mm. Note that DMRT-ML is identical to DMRT-QMS over the whole analyzed range of Do, as we stay in the Rayleigh range (see Picard et al., 2013), and despite the different formulation of the scattering coefficient. When the grain size becomes larger (Do > 0.6 mm, SSA < 11 $m^2\ kg^{-1}$), the HUT-nlayers T_B significantly decreases, because this model empirically considers multiple scattering and is based on the 1-flux RT simplification, leading to underestimate downward-propagated T_B and then upward reflected and backscattered signal. Multiple scattering increasing with grain size tends to increase the upward radiation, compensating for the T_B attenuation.

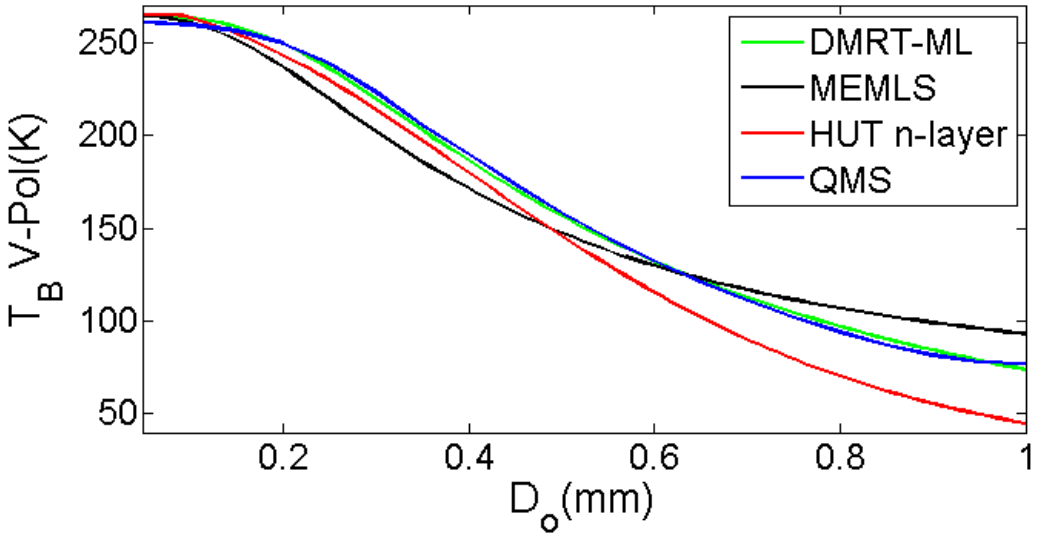

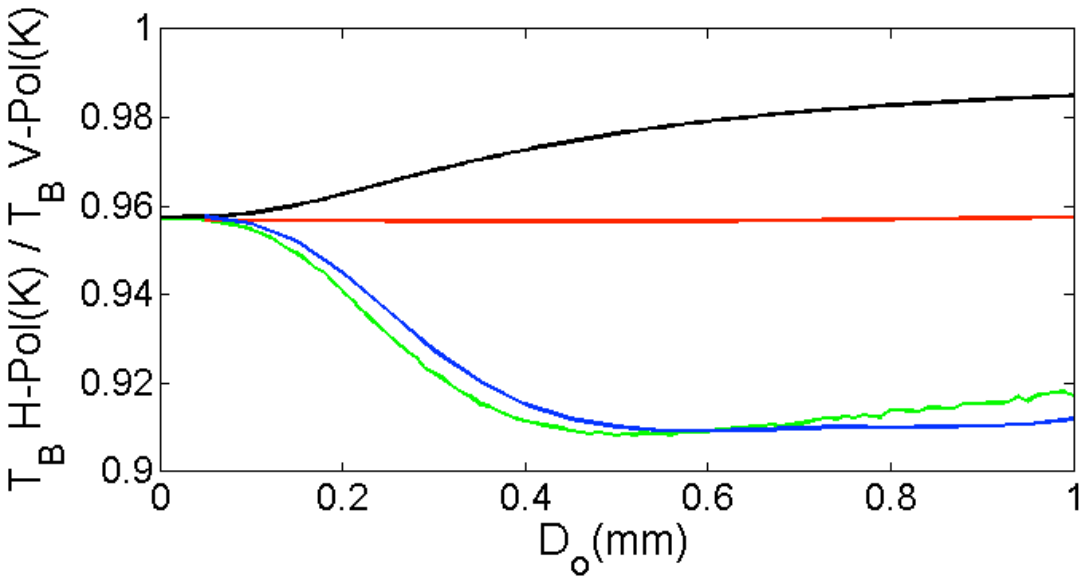

Fig. 2 T_B variation at 37 GHz as a function of the optical diameter (Do) of grain size for the four models. Top: T_B at the Vertical polarization; Bottom: Polarization ratio (H-pol/V-pol). Simulations performed using Eq. 11 for the snow grain size definitions and the Wegmüller and Mätzler (1999) soil model (Table 1); Soil temperature = 273 K; soil roughness = 0.19 cm, dielectric permittivity = 4.53 and the polarization reflectivity factor beta = 1.1 (Montpetit et al., 2015a); snow density = 250 kg.m^{-3}; snow depth = 1 m; Snow temperature = 263 K; no stickiness and no ice lens. The incidence angle of T_B simulations is 55°.

The main polarization effects arise from reflections at layer interfaces, and are at their maximum near the Brewster angle (around 55° at 37 GHz), leading to a significant decrease of the T_B (H-pol) with incidence angle, while T_B V-pol is weakly independent of the incidence angle. Fig. 2 (bottom) shows the Polarization Ratio (PR = T_B H-pol/T_B V-pol) variations for the four models as a function of the optical grain size simulated for a fixed incidence angle of 55°. DMRT-ML and DMRT-QMS are also identical in this case. The HUT model practically neglects the scattering polarization variations with growing grain size, while DMRT-ML/-QMS and MEMLS models show different trends in PR variations with grain size. The MEMLS volume scattering in snow is slightly sensitive to polarization (Wiesmann et al., 1998) with a weak PR increase of 2% when

428 the grain size increases between Do = 0.1 to 0.6 mm, while DMRT-ML/-QMS decreases by 4%,
429 leading to a difference of about 7% compared to MEMLS for grain sizes above 0.6 mm (Fig. 2,
430 bottom).
431 For a given fixed density, the polarization is modulated by 2 mechanisms: snow scattering and
432 interface reflection. As snow-air interface reflections are similarly treated in each model
433 (assuming Fresnel's reflection) and because the density remains constant in these simulations, the
434 differences between the three types of models (DMRT-ML/-QMS; HUT-nlayers and MEMLS)
435 result from the differences in the radiative transfer solution. As a matter of fact, polarization
436 effects are generated by volume scattering driven by the granular structure of the medium, i.e. by
437 a combined effect of snow grain size and density (see Mätzler, 1997) and also of stickiness for
438 DMRT-ML/-QMS (see Picard et al., 2013). The observed differences in PR variations in Fig. 2
439 (bottom) could thus likely governed by differences between the radiative transfer processing of
440 the diffuse scattering component of the signal. The results for lower incidence angles (i.e. not
441 Brewster) are similar.
442 We performed simulations (not shown) using a new model (in progress, unpublished) using the
443 same N-flux solver used in DMRT-ML but which can compute scattering coefficients with either
444 the DMRT theory (as in DMRT-ML and DMRT-QMS) or IBA (as in MEMLS). In both cases,
445 assuming the same scattering theory, the results show a decrease of the PR with increasing Do,
446 while the MEMLS-IBA (6-flux) shows an increase of the PR. This suggests that the radiative
447 transfer processing, specifically 6-flux versus N-flux, could be the cause of the different
448 behaviors observed in Figure 2 (bottom), but further exploration of the role of the solver is
449 needed,
450
451 The patterns of T_B variation with snow density show similar behaviors between models but at
452 different amplitudes (Fig. 3). Here, Do is considered constant and equal to 0.25 mm. Over the
453 range of density variation shown, below 400 kg m^{-3} (i.e. below 44% fractional volume), at

vertical polarization, DMRT-ML/-QMS shows a greater sensitivity, ΔT_B V-pol of 40 K for density from 150 to 300 kg.m^{-3}, than MEMLS and HUT which vary slightly. For low snow density between 150 and 200 kg m^{-3} the four models are similar, but at a high snow density of 400 kg m^{-3}, the T_B(V-pol) difference between DMRT-ML/-QMS and MEMLS is 28.5 K. (and 21.3 K at H polarization) (Fig. 3, top). For coarser grain size (not shown), the differences in T_B V-pol versus density variations between models are amplified, due to the difference in scattering processing in each model.

PR variations in relation to density show parallel trends (Fig. 3, bottom), but the decrease in PR when density increases shows significant differences in slope values for each model (more than 2% difference at low density for MEMLS and HUT compared to both DMRT models). For high densities (near 400 kg/m^3), this decrease is greater with DMRT-ML than DMRT-QMS.

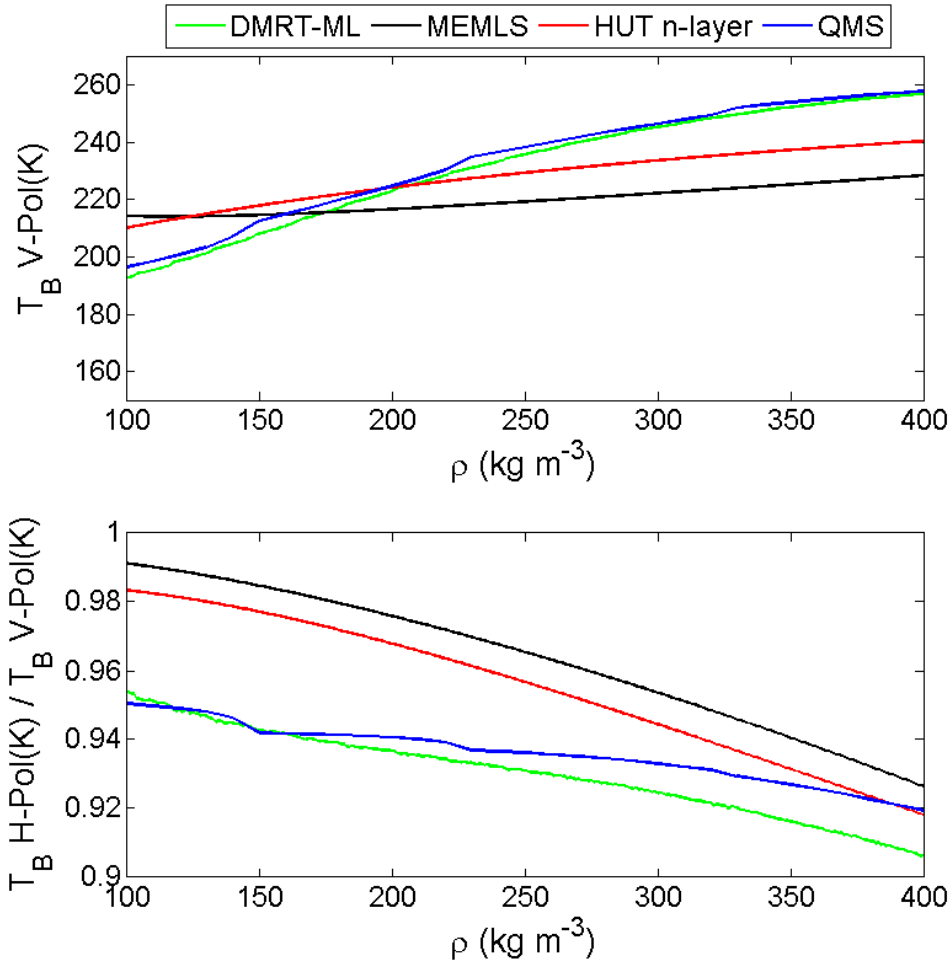

Fig. 3 Same as Fig. 2, but for density (Do = 0.25 mm).

467

468 T_B H-pol varies as a function of density change between interface layers, mainly from reflection
469 at the snow-air interface, and of snow scattering (grain size). Since Fresnel reflection is
470 considered here, surface reflection depends on the snow dielectric constant and thus the density.
471 Assuming a constant grain size (as in Fig. 3), as density increases, the reflection coefficient
472 increases and T_B H-pol decreases, leading to the decrease in PR (as T_B V-pol is relatively
473 constant at the Brewster angle). In other words, where snowpack evolution features slow
474 metamorphism as is observed in Antarctica, PR clearly decreases with density. This was shown
475 by Picard et al. (2014) from surface-based measurements at Dome Concordia (East Antarctica).
476 Champollion et al. (2013) also showed that the observed 2000-2010 AMSR-E PR increase was in
477 agreement with the observed decreasing surface snow density, also at Dome Concordia.
478 However, when the snowpack evolves during the winter through various metamorphic processes
479 (increasing grain size), increasing layering (alternation of high- and low-density layers) and
480 increasing density processes, PR direction changes over time appear less clear. Moreover, the
481 surface roughness would produce a more diffuse scattering distribution, leading to weaker
482 polarization, while ice layers or wind-slab snow crusts lead to a significant degree of polarization
483 (e.g. Mätzler, 1982, 1994; Grenfell and Putkonen, 2008; Dolant et al., 2016). In general, since
484 surface density and state are the most important characteristics influencing polarization, one
485 expects a decrease in PR with time from snowfall. The DMRT simulations showed a PR decrease
486 for both increasing grain size and density processes in the synthetic cases considered here (Fig. 2
487 and 3), while MEMLS and HUT show a PR decrease only as a function of increasing density.
488

489 The third sensitivity analysis (Fig. 4) shows the effect of a thin ice layer put at the top of the
490 snowpack for the four models. At V-pol, there are almost no T_B variations due to ice lens while
491 TB H-pol is reduced by up to 65 K when an ice lens is introduced. The stronger decrease in H-pol
492 (ice lens vs. no ice) compared to the one at V-pol comes from the higher sensitivity to layer

493 interface reflectivity at H-pol. Note that, in Fig. 4, the differences in TB V-pol amplitudes
494 between models result from the configuration (Do and density) used for the simulations (see Fig.
495 2 and 3). Moreover, ice layer thickness variations have no impact on T_B variation, except when
496 using the MEMLS model for thin ice layers. Around D_{ice} = 0.125 mm, MEMLS is as much as 43
497 K lower at H-pol than the DMRT and HUT models. This significant T_B decrease simulated by
498 MEMLS for H polarization that appears for ice thickness under λ/2 is due to the coherent
499 reflection that dominates the microwave behavior for layers of the size λ/4 (Weismann and
500 Mätzler, 1999). The DMRT-ML and HUT-nlayers models do not take into account this
501 attenuation effect of the quarter-wavelength resonance. In practice, as the ice layer thickness
502 spatially varies in the footprint of the sensor (Rutter et al., 2014), such effects are generally less
503 pronounced than in simulations, but can be clearly observed for thin ice lenses on or in the
504 snowpack (see Montpetit et al., 2013; Roy et al., 2016).

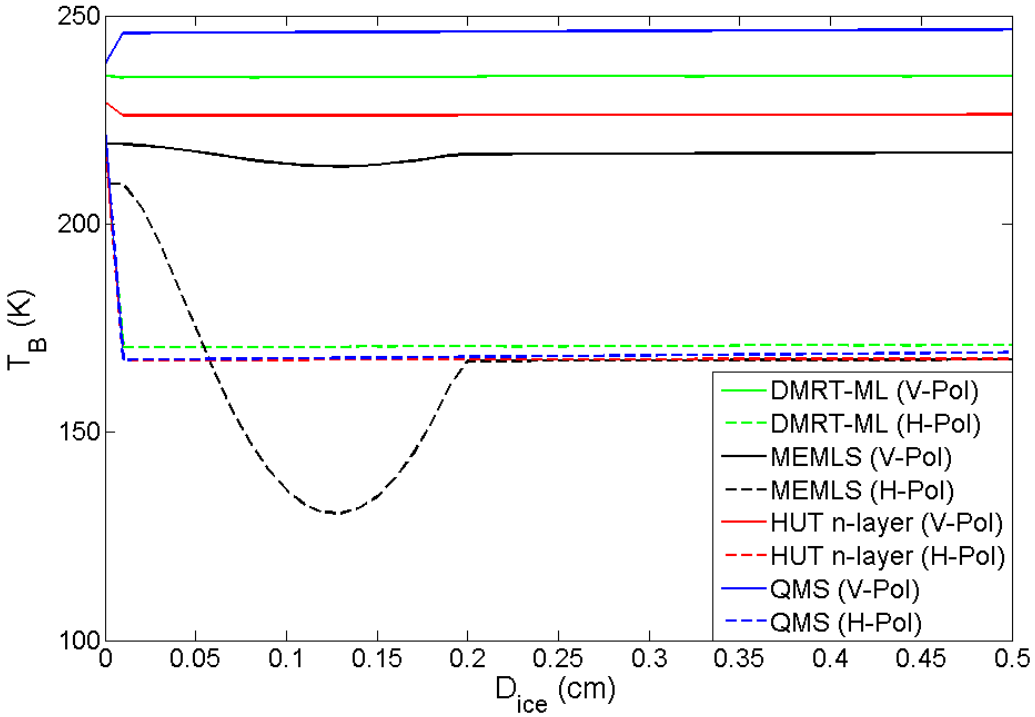

505
506 **Fig. 4** T_B variation at 37 GHz as a function of an ice layer thickness (D_{ice}) put on the top of the
507 snowpack for the four models (full lines: V-pol; dotted lines: H-pol). Snowpack and soil
508 properties are the same as in Fig. 2 and 3 (Do = 0.25 mm and density = 250 $kg.m^{-3}$). Ice lens

509 density = 917 kg m^{-3} and ice lens temperature is the same as snow temperature.

510

511 ***4.2 Snow grain database comparison analysis***

512 We analyzed 159 photographed plates from the 32 studied snowpits, corresponding to a total of
513 36,384 digitized grains with an average of 229 grains per plate. For each plate, we considered the
514 mean maximum dimension of all the grains on the plate (D_{max}). For each corresponding layer, we
515 also measured the snow SSA and density. It is well known that the relationship between Do and
516 D_{max} is not one-to-one (see Langlois et al., 2010; Leppänen et al., 2015). However, in order to
517 evaluate the consistency of the datasets, Fig. 5 shows the relationship between the calculated
518 correlation length derived from SSA and density measurements (Eq. 5, $\phi = 1$) and the
519 corresponding mean D_{max} for all the samples. The results show that this relationship appears
520 somewhat scattered as expected, and more linear rather than the logarithmic relationship
521 suggested by Mätzler (2002). But note that, for the latter case (for 20 samples), D_{max} values were
522 visually determined, whereas, in our case, D_{max} were derived from digitized contours. The
523 digitization, the very large number of data and also the computation of the mean values (over
524 hundreds of grains) could explain that our D_{max} values are different than those visually
525 determined. The digitization of grain size is considered as a more reproducible and more precise
526 approach. We also considered (not shown) median values instead of arithmetic means that did not
527 give significant differences. On the other hand, the correlation lengths in the Mätzler (2002)
528 database were measured (micro-CT) whereas we derived this parameter from SSA and density
529 measurements. The reason for the differences between these micro-structure metrics (D_{max}, SSA,
530 correlation length), discussed for example by Löwe and Picard (2015), and which may also result
531 from differences in snow types (alpine, boreal, arctic), is beyond the scope of this paper. This
532 unique database (coincident values of Do, pc and D_{max}) was used to provide specific inputs to
533 drive each model considered in order to simulate the brightness temperatures.

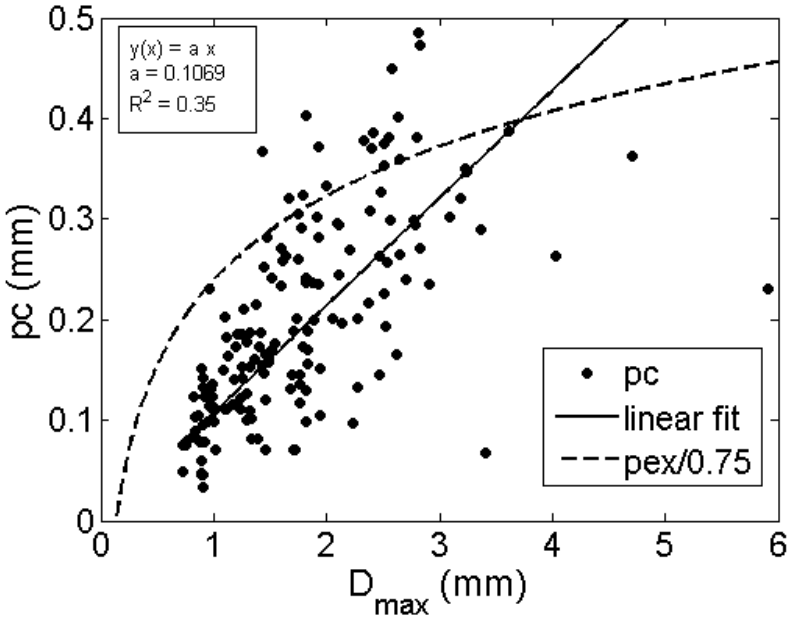

534

535 **Fig. 5** Relationship between the correlation length derived from SSA and density measurements
536 (p_c, calculated with Eq. 5, $\phi = 1$) and the mean maximum geometrical extent of the grains (D_{max})
537 measured by digitized photographs of snow grains (each point of this graph corresponds in
538 average to 229 digitized grains per sample). The dotted curve corresponds to the logarithmic
539 relationship observed by Mätzler (2002).

540

541 **4.3 Model comparison using measured inputs**

542 As DMRT-QMS is very similar to DMRT-ML, only three models are considered in the
543 following: DMRT-ML, HUT-nlayers and MEMLS. For all the sites described in the Table 4, Fig.
544 6 compares the 3 model simulations against surface-based measured brightness temperatures with
545 exactly the same soil parameters (Table 3), and for the snow microstructure metrics derived either
546 from SSA or D_{max} measurements. DMRT-ML (Fig. 6a), HUT_Do (Fig. 6b) and MEMLS_Do
547 (Fig. 6c) were driven by the scaled optical diameter of snow grain derived from SSA
548 measurements. The HUT_D_{max} simulations (Fig. 6d) were driven by D_{max} measurements using an
549 optimized scaling factor (see Section 2). Using D_{max} measurements, two inputs were also
550 considered for MEMLS simulations: 1) MEMLS_D_{max}_p_{ex} (Fig. 6e) based on the Mätzler
551 relationship (Durand et al., 2008, Eq. 7, see Fig. 5); and 2) MEMLS_Dmax_lin (Fig. 6f) based on

552 the correlation length estimated by the observed linear relationship shown in Fig. 5. These model
553 inputs are summarized in Table 5.
554
555 The root mean square errors (RMSE) and the biases are compared in Table 6 and shown in Fig. 7
556 for the three frequencies (11, 19 and 37 GHz) and each polarization. Note that the full set of input
557 snow properties and 11 GHz radiometer measurements are only available for two sites, hence, the
558 analysis focuses on 19 and 37 GHz.
559
560
561 **Table 5** Summary of the inputs used for the model simulations. The corresponding equations
562 (Eq.) are explained in Section 2.

Model configuration	Grain size measurements	Input parameters	Eq.	Fig.
DMRT-ML	SSA	$D'o = 6.10^3\ 3.3/(\rho_{ice} \cdot SSA)$	2	6a
MEMLS_Do	SSA	$p'_c = 4.10^3\ 1.3(1 - \nu)/(\rho_{ice} \cdot SSA)$	6	6c
MEMLS_D_{max}_p_{ex}	D_{max}	- $p_{ex} = 0.18 + 0.09 \ln(D_{max})$ for $\nu > 0.2$ and $D_{max} > 0.125$ mm - $p_{ex} = 0.05 \pm 0.017$ otherwise	7	6e
MEMLS_D_{max}_lin	D_{max}	$p_c = 0.1069$ Dmax	Fig. 5	6f
HUT_Do	SSA	$Do_{eff} = 6.10^3\ 3.7/(\rho_{ice} \bullet SSA)$	9	6b
HUT_D_{max}	D_{max}	$D_{max,eff} = 0.5\ D_{max}$	-	6d

563
564
565
566
567

568 **Table 6** Bias (B) and RMSE (R) (K) between simulated and measured T_Bs for each frequency
569 and polarization and for each model driven by specific inputs (described in Table 5). Bold:
570 minimum bias and RMSE values of each line respectively (but not necessarily statistically
571 significant).

Model	**DMRT-ML**		**MEMLS**						**HUT**			
Inputs	Do ϕ=3.3		Do ϕ=1.3		D_{max}_lin (Fig. 5)		D_{max}_p_{ex} Eq.7		Do ϕ=3.7		D_{max} ϕ=0.5	
	B	R	B	R	B	R	B	R	B	R	B	R
11V	2.1	2.5	5.5	5.8	5.5	5.5	7.8	7.8	-2.1	2.4	**-1.1**	**1.7**
11H	-7.3	7.5	-4.1	4.5	-3.9	4.9	**-2.6**	**4.1**	-10.0	10.3	-9.1	9.4
19V	16.0	19.4	**0.1**	**11.4**	6.2	14.5	15.0	18.2	13.8	18.7	13.6	17.8
19H	14.7	23.0	**2.9**	**17.0**	7.8	18.8	15.0	23.7	8.5	27.5	13.4	22.4
37V	11.0	25.3	-10.8	**21.6**	-10.8	26.7	-10.8	24.4	11.3	32.4	**9.6**	30.8
37H	7.5	20.1	-4.9	**16.4**	**-3.3**	19.9	9.0	21.4	8.5	27.5	6.7	23.4
All	7.3	16.3	-3.1	12.8	0.3	15.0	5.6	16.6	5.9	19.1	5.5	17.6

572
573
574 For the 32 analyzed snowpits, the overall results at 19 and 37 GHz for the 6 model configurations
575 show mean bias values of the order of 6 K, ranging from -10.8 to 16 K depending on the model,
576 configuration and frequency considered. The mean RMSE value is of the order of 20 K (19 GHz)
577 and 24 K (37 GHz), ranging from 11.4 to 32.4 K. Large differences in bias appear between
578 models (MEMLS with negative biases), and no significant differences in bias or RMSE can be
579 seen between polarizations. Note that except for HUT_Dmax (0.5 • Dmax), the models were not
580 specifically optimized for the new cases considered in this study, since the used scaling factors
581 were derived from previous publications over different sites.
582
583

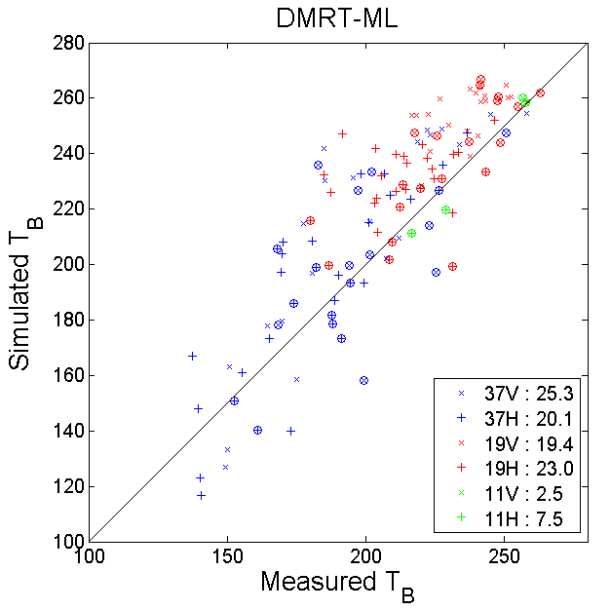
DMRT-ML
Simulated T_B
Measured T_B
37V : 25.3
37H : 20.1
19V : 19.4
19H : 23.0
11V : 2.5
11H : 7.5

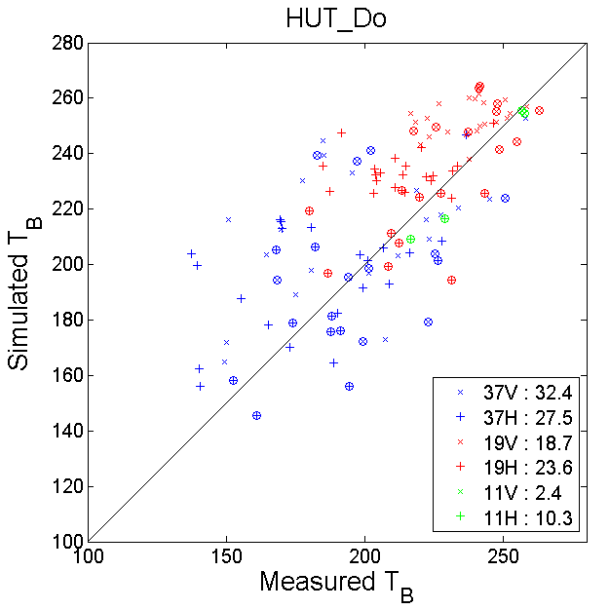
HUT_Do
Simulated T_B
Measured T_B
37V : 32.4
37H : 27.5
19V : 18.7
19H : 23.6
11V : 2.4
11H : 10.3

584

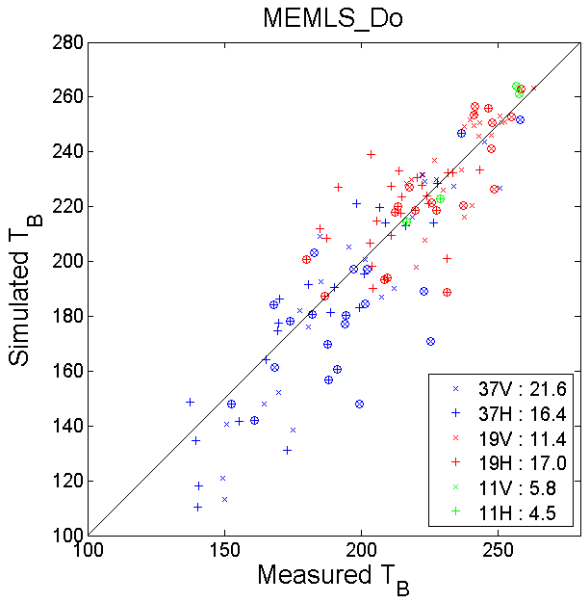
MEMLS_Do
Simulated T_B
Measured T_B
37V : 21.6
37H : 16.4
19V : 11.4
19H : 17.0
11V : 5.8
11H : 4.5

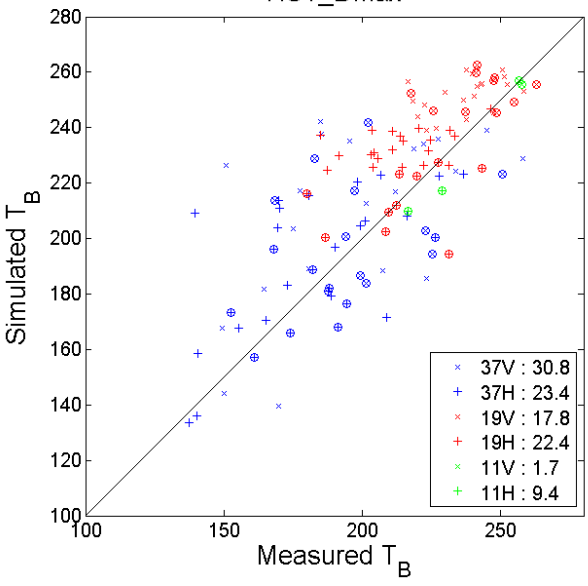
HUT_Dmax
Simulated T_B
Measured T_B
37V : 30.8
37H : 23.4
19V : 17.8
19H : 22.4
11V : 1.7
11H : 9.4

585

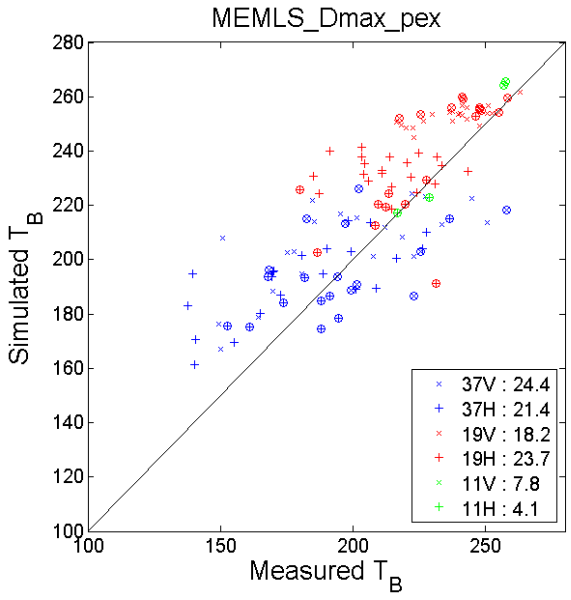
MEMLS_Dmax_pex
Simulated T_B
Measured T_B
37V : 24.4
37H : 21.4
19V : 18.2
19H : 23.7
11V : 7.8
11H : 4.1

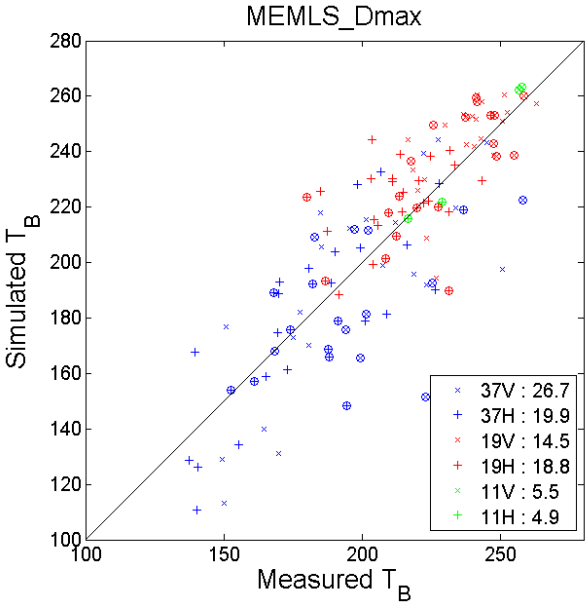
MEMLS_Dmax
Simulated T_B
Measured T_B
37V : 26.7
37H : 19.9
19V : 14.5
19H : 18.8
11V : 5.5
11H : 4.9

586

Fig. 6 Scatterplot comparing simulated brightness temperatures against measurements for each frequency and polarization for all the sites (described in Table 4). Circled symbols represent sites that included ice lenses. a: DMRT, b: HUT_Do (right); c: MEMLS_Do; d: HUT_Dmax; e: MEMLS_Dmax_p_{ex}; f: MEMLS_Dmax_lin. Input parameters are listed in Table 5. Values given in the figures correspond to the RMSE in Kelvin (reported in Table 6).

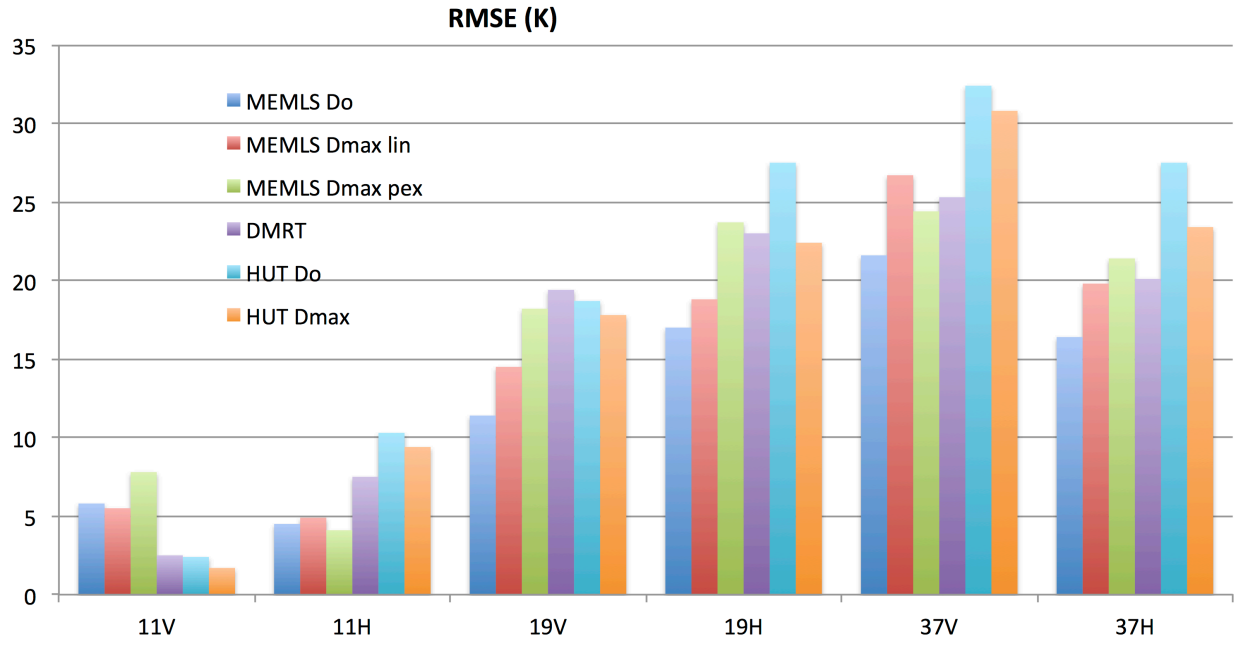

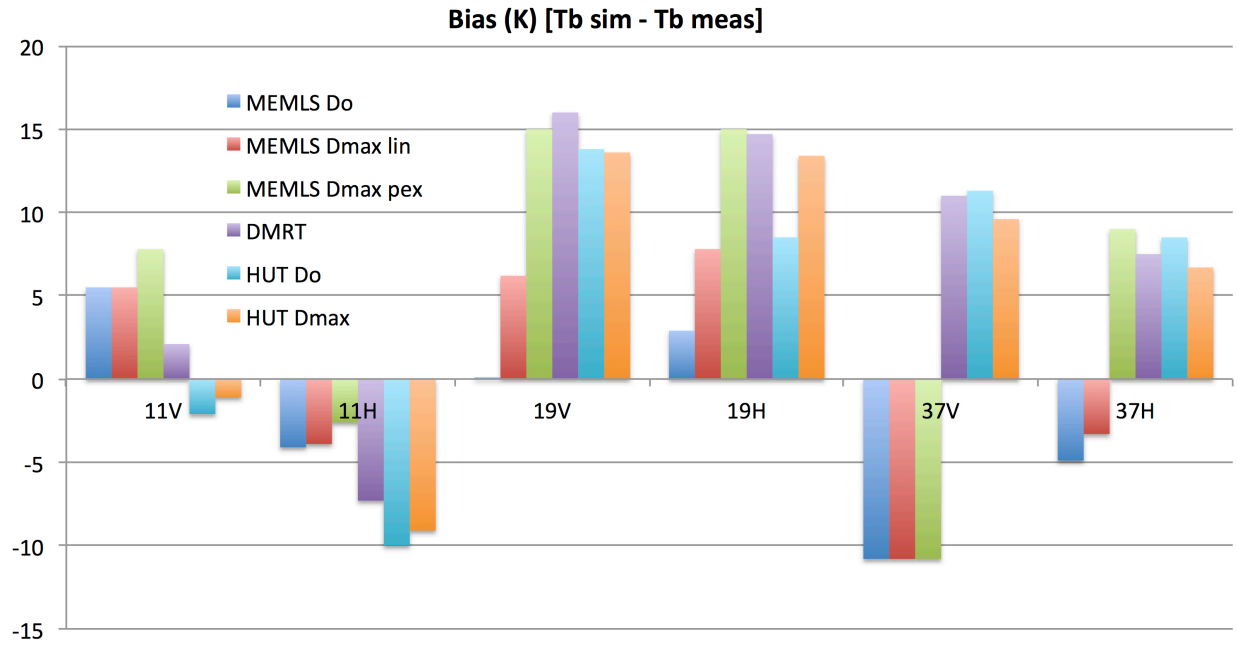

595 **Fig. 7** Comparison between the RMSE and biases for the 6 model configurations. The
596 corresponding values are given in Table 6.
597
598 MEMLS_Do seems to give slightly better results (mean RMSE of 14 K and 19 K, respectively at
599 19 and 37 GHz, for both polarizations) relative to other configurations and models (Fig. 6, 7 and
600 Table 6). DMRT-ML results show a mean RMSE of 21 K (19 GHz) and 23 K (37 GHz) in this
601 study, although we obtained better results for 45 other Arctic and Subarctic snowpits with the
602 same parameterization (mean RMSE of 10 K (19 GHz) and 12 K (at 37 GHz), see Roy et al.,
603 2016). The HUT model shows a lesser agreement at 37 GHz (mean RMSE of 30 K and 27 K
604 respectively for the Do and D_{max} configuration).
605
606 MEMLS tends to underestimate the T_B at 37 GHz V-pol (negative bias), while the other models
607 tend to overestimate the simulated T_B (positive bias). This is in accordance with the comparison
608 using synthetic snowpacks (see Fig. 2, top), showing lower MEMLS T_B compared to DMRT and
609 HUT for a large range of grain sizes.
610
611 Among the three analyzed MEMLS versions, it appears that MEMLS_Do performs best,
612 compared to the D_{max}-based simulations (an average RMSE at 19 and 37 GHz of 16.6 K, 20 K
613 and 22 K for respectively the MEMLS_Do, _D_{max}_lin and _D_{max}_p_{ex} configurations). As
614 expected, the HUT model provides a slightly lower RMSE when using D_{max} (23.6 K) compared
615 to HUT_Do (26.5 K). Moreover, at 37 GHz, DMRT using SSA appears better than the HUT
616 model based on D_{max}. This confirms that the scaled SSA parameter is, in general, clearly better
617 than the D_{max} parameter for describing snow grain size for microwave radiometry no matter the
618 MEMLS or DMRT-ML model.
619
620

We showed (Fig. 4) that, for the synthetic snowpack, ice lens thickness within the snowpack could lead to significant differences in T_B among the models. Here, we accounted for the ice layer effects when they were observed in the snowpack, and the comparison shown in Fig. 6 does not exhibit systematic differences between snowpits with ice layers (10 sites/32, see Table 4) and those without ice layers. This first shows that ice layers can be adequately corrected for when their presence and particularly their position within the snowpit is known (see Montpetit et al., 2013; Roy et al, 2016), and secondly that ice layers cannot explain the differences in RMSE between models.

In terms of linear regression between simulated and measured T_B (coefficient of determination R^2 and slope of the regression), the model comparison (Table 7) also highlights the differences between models and configurations. Best results are obtained with DMRT-ML and MEMLS_Do, with a mean R^2 of the order of 0.75 – 0.79 for the 4 channels (T_B at 19 and 37 GHz and both polarizations). Results for these models are better at 37 GHz and with a slope slightly greater than 1, meaning that the models underestimate low T_B values at this frequency (T_B < ~170 K). Even if MEMLS_Dmax_lin is really better than MEMLS_Dmax_p_{ex} for both R^2 and slope parameters, MEMLS_Dmax_lin performs less well than MEMLS based on Do. The HUT model gives here the worst agreement against measurements. Note that, in all cases (Table 7), the T_B H-pol values at 19 GHz show the lowest correlations, likely due to non-optimized processing of stratification between the snow layer interfaces, assumed specular, and for the soil-snow interface (roughness, for example). The statistics at 11 GHz are not included because there are only 2 measurements, but are included in the overall linear regression.

Table 7 Comparison of linear regression parameters (coefficient of determination R^2 and slope of the regression) for simulated and measured T_B for the models shown in Fig. 6. All*: including 11 GHz at H-pol and V- pol.

Model	**DMRT-ML**		**MEMLS**						**HUT**			
Inputs	Do ϕ=3.3		Do ϕ=1.3		D_{max}_lin (Fig. 5)		D_{max} p_{ex} Eq.7		Do ϕ=3.7		D_{max} ϕ=0.5	
	R^2	Slope	R^2	Slope	R^2	Slope	R^2	Slope	R^2	Slope	R^2	Slope
19V	0.30	0.53	0.52	0.95	0.29	0.64	0.46	0.20	0.14	0.24	0.11	0.19
19H	0.13	0.33	0.23	0.47	0.17	0.39	0.03	0.12	0.05	0.18	0.05	0.17
37V	0.63	1.07	0.72	1.04	0.45	0.78	0.31	0.29	0.13	0.34	0.19	0.43
37H	0.73	1.19	0.78	1.10	0.58	0.88	0.48	0.36	0.22	0.45	0.34	0.58
All*	0.75	1.10	0.79	1.06	0.69	0.98	0.63	0.70	0.51	0.73	0.55	0.76

At least, we compared the simulated Polar Ratio (PR H/V) at 37 GHz to the measured PR. The results show similar performance between the models (mean RMSE of 0.055). Also, we cannot conclude about the effect of the grain size on the PR trend (as simulated in Fig. 2). This relates to the fact that the sites integrate a large range of density and Do values, while Fig. 2 assumes a constant density when Do varies.

5. Discussion and conclusion

Over a large set of Arctic, Subarctic and boreal snow datasets, we derived a unique comprehensive snow grain size metrics database. These metrics were defined, on the one hand, by their specific surface area (SSA, from IR reflectometry measurements), and, on the other hand, for the same snow samples, by their mean maximum geometrical extent, called D_{max}, obtained from digitized macrophotos of snow samples at each layer. Here, we did not estimate D_{max} size by visual inspection as is generally done, because of the subjectivity of that approach. The digitization of each snow grain distributed on a photographed plate is thought to be a more robust and objective approach. This dataset allowed us to compare ground-based measurements of brightness temperatures (T_B) to the simulated T_B using four models driven by their specific

667 metrics: DMRT-ML and -QMS with the optical diameter (Do) derived from SSA measurements;
668 the HUT model with D_{max}; and the MEMLS model driven by the correlation length which can be
669 estimated using both parameters (Do and D_{max}). We also tested the HUT model with Do, and we
670 compared MEMLS simulations based on 2 different relationships for correlation length
671 estimation. A total of six model configurations (Table 5) were thus analyzed (Fig. 6, 7 and Table
672 6).
673
674 Whatever the model considered, the scatterplots between simulated and measured T_B show
675 somewhat large scatters (Fig. 6) due to the inherent uncertainties on all the parameters that affect
676 the emitted signal, i.e. soil (temperature, dielectric permittivity and roughness), snow density
677 stratification, snow temperature profile and snow grain size stratification (Roy et al., 2016;
678 Durand et al., 2008). The obtained root mean square error between simulated and measured T_B
679 are in the same range of values shown in previous studies that considered the same models (Roy
680 et al., 2016; Pan et al., 2016; Löwe and Picard, 2015; Roy et al. 2013; Lemmetyinen et al.,
681 2010b). The results analyzed here are thus representative of errors commonly obtained for Arctic
682 and Subarctic snows with these models. But this is the first time that these models were
683 compared with their specific snow microstructure input data for which they were defined. These
684 results confirm first that each metric, Do as well as pc and D_{max}, must be scaled in order to
685 minimize the RMSE between simulated and measured T_B. This aspect was discussed and partly
686 explained in previous papers (Löwe and Picard, 2015; Roy et al. 2013; Kontu and Pulliainen,
687 2010). Secondly, the results show that the snow microstructure metric based on Do appears to
688 give better results than the metric defined by D_{max} (Table 6). This may be due to the fact that
689 microwave scattering is more directly related to Do than to D_{max}. Also, even if the shadow box
690 used to measure D_{max}, is more accurate than visual estimates, the Do value, derived from snow
691 SSA measurements, could give a better estimate of the effective mean size over the grain size
692 distribution per layer than the mean value of D_{max} measurements.

It is difficult to conclude on the performance of DMRT-ML, HUT and MEMLS due to the large observed scatter on simulations, although the MEMLS model appears here slightly better for the snowpits analyzed in this study. We found a mean RMSE at high frequencies (19 and 37 GHz) of 16.6 K, 22.0 K and 23 K respectively for MEMLS_Do, DMRT-ML and HUT_D_{max}. However, as mentioned above, a specific optimization could have been made on the input parameters for each model (on the ϕ scaling factors) that would have a different effect on the models and change the results comparison. This scaling factor may also depend on the types of snow, i.e. on metamorphism processes and shape (see Löwe and Picard, 2015; Krol and Löwe, 2016). However, the comparison shown here between the four models using a synthetic snowpack (Fig. 2, 3 and 4) clearly shows the intrinsic difference in radiative transfer behavior as a function of grain size, density and ice lens variations within the snowpack, in particular for the polarization ratio (T_B H-pol / T_B V-pol).

In conclusion, to date, from a practical point of view using in-situ measurements of snow properties, this paper shows that the SSA parameter appears to be the most relevant parameter for characterizing snow microstructure, even if it must be scaled to be used for microwave simulations. Snow tomography could give more precise microstructure characterization but requires significant processing time. When suitably scaled for each model (MEMLS and DMRT-ML), the SSA parameter produces the same order of error magnitude in simulated brightness temperature. From a physical perspective, Löwe and Picard (2015) showed that MEMLS and DMRT-ML are in fact very similar.

Acknowledgements

This study was supported by the National Sciences and Engineering Research Council of Canada (NSERC), the Canadian Foundation for Innovation, Environment Canada, NASA-Goddard (L.B.)

719 and by the Programme de développement de partenariats stratégiques en matière d'enseignement
720 et de recherche of the Conseil franco-québécois de la coopération universitaire, a France-Québec
721 research collaboration. The authors would like to thank Patrick Cliche and Miroslav Chum for
722 creating the Shadow-box, all participants to the field works for their contributions to obtain the
723 ground-based measurements, and Peter Toose and Chris Derksen (Environment Canada) for
724 providing part of the Churchill data.
725

726 **References**

727 Armstrong, R., & Brodzik, M. (2002). Hemispheric-scale comparison and evaluation of passive-
728 microwave snow algorithms. *Annals of Glaciology*, 34, 38–44.
729 Asmus K.W. and C. Grant (1999). "Surface based radiometer (SBR) data acquisition system,"
730 *Int. J. Remote Sens.*, 20(15/16), 3125–3129.
731 Brucker, L., Picard, G., Arnaud, L., Barnola, J.M., Schneebeli, M., Brunjail, H., Lefebvre, E. and
732 Fily, M. (2011), Modeling time series of microwave brightness temperature at Dome C,
733 Antarctica, using vertically resolved snow temperature and microstructure measurements. *J. of*
734 *Glaciology*, 57(201), 171-182.
735 Champollion, N., Picard, G., Arnaud, L., Lefebvre, E., and Fily, M.: Hoar crystal development
736 and disappearance at Dome C, Antarctica: observation by near-infrared photography and
737 passive microwave satellite, *The Cryosphere*, 7, 1247-1262, doi:10.5194/tc-7-1247-2013.
738 Chang W., S. Tan, J. Lemmetyinen, L. Tsang, X. Xu, X. Li and S. Yueh (2014). Dense Media
739 Radiative Transfer Applied To SnowScat and SnowSAR, *IEEE Journal of Selected Topics in*
740 *Applied Earth Observations and Remote Sensing*, 7(9), 3811 – 3825.
741 Colbeck S., E. Akitaya, R. Armstrong, H. Gubler, J. Lafeuille, K. Lied, D. McClung, and E.
742 Morris (1990), *The International Classification for Seasonal Snow on the Ground*.
743 Wallingford, U.K.: Int. Commission Snow Ice Int. Assoc. Sci. Hydrol., Working Group Snow
744 Classification.

745 Courtemanche B., B. Montpetit, A. Royer and A. Roy (2015). Creation of a lambertian
746 microwave surface for retrieving the downwelling contribution in ground-based radiometric
747 measurements. *IEEE Geoscience and Remote Sensing Letters*, 12(3), 462-466.
748 Dolant C., A. Langlois, B. Montpetit, L. Brucker, A. Roy and A. Royer (2016). Development of
749 a rain-on-snow detection algorithm using passive microwave radiometry. *Hydrol.*
750 *Process.*, Published online in Wiley Online Library, DOI: 10.1002/hyp.10828
751 Domine, F., Albert, M. , Huthwelker, T. , Jacobi, H. W. , Kokhanovsky, A. A. , Lehning, M. ,
752 Picard, G. and Simpson, W. R. (2008): Snow physics as relevant to snow photochemistry ,
753 *Atmospheric Chemistry and Physics*, 8 , 171-208.
754 Dupont, F., Picard, G., Royer, A., Fily, M., Roy, A., Langlois, A., and Champollion, N. (2014).
755 Modeling the Microwave Emission of Bubbly Ice: Applications to Blue Ice and Superimposed
756 Ice in the Antarctic and Arctic, *IEEE T. Geosci. Remote*, 52, 6639–6651,
757 doi:10.1109/TGRS.2014.2299829.
758 Durand, M., E. J. Kim, and S. A. Margulis (2008), Quantifying uncertainty in modeling snow
759 microwave radiance for a mountain snowpack at the point-scale, including stratigraphic
760 effects, *IEEE Trans. Geosci. Remote Sens.*, 46, 1753–1767.
761 Fierz, C., Armstrong, R. L., Durand, Y., Etchevers, P., Greene, E., McClung, D. M., Nishimura,
762 K., Satyawali, P. K., and Sokratov, S. (2009). *The International Classification for Seasonal*
763 *Snow on the Ground*, IHP-VII Technical Documents in Hydrology, 83, IACS Contribution (1),
764 UNESCO-IHP, Paris.
765 Gallet, J.-C., Domine, F., Zender, C. S., and Picard, G. (2009). Measurement of the specific
766 surface area of snow using infrared reflectance in an integrating sphere at 1310 and 1550 nm,
767 *The Cryosphere*, 3, 167–182, doi:10.5194/tc-3-167-2009.
768 Grenfell T.C. and Putkonen J. (2008). A method for the detection of the severe rain- on-snow
769 event on Banks Island, using passive microwave remote sensing. *Water Resources Research*
770 44:W03425: DOI:10.1029/2007WR005929.

771 Grody, N. (2008). Relationship between snow parameters and microwave satellite measurements:
772 Theory compared with Advanced Mi- crowave Sounding Unit observations from 23 to 150
773 GHz, *J. Geophys. Res.*, 113, 17 pp., doi:10.1029/2007JD009685.
774 Hallikainen M.T., F. T. Ulaby, and T. E. Van Deventer (1987). "Extinction behavior of dry snow
775 in the 18-to 90-GHz range," *IEEE Trans. on Geoscience and Remote Sensing*, 6, 737–745.
776 Huang S. and L. Tsang (2012). Electromagnetic Scattering of Randomly Rough Soil Surfaces
777 Based on Numerical Solutions of Maxwell Solutions of Maxwell Equations in Three-
778 Dimensional Simulations Using a Hybrid UV/PBTG/SMCG Method, *IEEE Trans. on*
779 *Geoscience and Remote Sensing*, 50(10), 4025-4035.
780 Jin, Y. Q. (1994). *Electromagnetic scattering modelling for quantitative remote sensing*, World
781 Scientific, Singapore, 1994.
782 Kelly, R., Chang, A., Tsang, L., & Foster, J. (2003). A prototype AMSR-E global snow area and
783 snow depth algorithm. *IEEE Trans. on Geoscience and Remote Sensing*, 41(2), 230–242.
784 Kontu, A. and J. Pulliainen (2010). Simulation of spaceborne microwave radiometer mea-
785 surements of snow cover using in situ data and brightness temperature modeling. *IEEE*
786 *Transactions on Geoscience and Remote Sensing*, 48(3), 1031–1044.
787 Krol Q. and H. Löwe (2016). Relating optical and microwave grain metrics of snow: The
788 relevance of grain shape. *The Cryosphere Discuss.*, doi:10.5194/tc-2016-119.
789 Langlois A. (2015). *Applications of the PR Series Radiometers for Cryospheric and Soil*
790 *Moisture*. Research, Technical Report, © Radiometrics Corporation, 2015, 40p.
791 Langlois, A., A. Royer, B. Montpetit, G. Picard, L. Brucker, L. Arnaud, P. Harvey-Collard, M.
792 Fily and K. Goïta (2010). On the relationship between snow grain morphology and in-situ near
793 infrared calibrated reflectance photographs. *Cold Regions Science and Tech.*, 61(1), 34-42.
794 Lemmetyinen J., A. Kontu, A. Rees, C. Derksen, and J. T. Pulliainen (2010b). Comparison of
795 multiple layer snow emission models," presented at the *2010 11th Specialist Meeting on*
796 *Microwave Radiometry and Remote Sensing of the Environment (MicroRad)*, Washington,

797 DC, 2010, pp. 99–103.
798 Lemmetyinen J., C. Derksen, P. Toose, M. Proksch, J. Pulliainen, A. Kontu, K. Rautiainen, J.
799 Seppänen, M. Hallikainen (2015). Simulating seasonally and spatially varying snow cover
800 brightness temperature using HUT snow emission model and retrieval of a microwave
801 effective grain size. *Remote Sensing of Environment* 156, 71–95.
802 Lemmetyinen, J., Pulliainen, J., Rees, A., Kontu, A., Qiu, Y., & Derksen, C. (2010a). Multiple
803 layer adaptation of the HUT snow emission model: comparison with experimental data. *IEEE*
804 *Transactions on Geoscience and Remote Sensing*, 48, 2781–2794.
805 Leppänen, L., A. Kontu, J. Vehviläinen, J. Lemmetyinen, and J. Pulliainen (2015). Comparison
806 of traditional and optical grain size field measurements with SNOWPACK simulations in a
807 taiga snowpack. *J. Glaciol.*, 61(225), 151-162.
808 Lesaffre B., E. Pougatch et E. Martin (1997). Détermination objective des caractéristiques des
809 grains de neige à partir d'images. *La Houille Blanche*, 7, 76-82, DOI: 10.1051/lhb/1997068.
810 Liang D., X. Xu, L. Tsang, K. M. Andreadis and E. G. Josberger (2008). The effects of layers in
811 dry snow on its passive microwave emissions using dense media radiative transfer theory
812 based on the quasicrystalline approximation (QCA/DMRT), *IEEE Trans. Geos. Rem. Sens.*,
813 46(11), 3663-3671.
814 Liebe, H. (1989). MPM: An atmospheric millimeter-wave propagation model. *Int. J. of Infrared*
815 *and Millimeter Waves*, 10(6), 631–650.
816 Löwe, H. and Picard, G. (2015). Microwave scattering coefficient of snow in MEMLS and
817 DMRT-ML revisited: the relevance of sticky hard spheres and tomography-based estimates of
818 stickiness, *The Cryosphere*, 9, 2101-2117.
819 Löwe, H., Riche, F., and Schneebeli, M. (2013), A general treatment of snow microstructure
820 exemplified by an improved relation for thermal conductivity, *The Cryosphere*, 7, 1473–1480.
821 Mätzler C. and A. Wiesmann (2014). *Microwave Emission Model of Layered*
822 *Snowpacks; Documentation for MEMLS, Version 3*. Institute of Applied Physics - University

of Bern Sidlerstrasse 5, 3012 Bern, Switzerland, 26 pp.

Mätzler C. (Ed.), P.W. Rosenkranz, A. Battaglia and J.P. Wigneron (Co-Eds.) (2006). Thermal Microwave Radiation - Applications for Remote Sensing, *IET Electromagnetic Waves Serie*s 52, London, UK.

Mätzler C. (1996, 2004). "*Notes on microwave radiation from snow samples and from a layered snowpack*", IAP Research Report 96-9, University of Bern, Switzerland, (1996).

Mätzler, C. (2002), Relation between grain-size and correlation length of snow, *J. Glaciol.*, 48, 461–466.

Mätzler C. and A. Wiesmann (1999). "Extension of the Microwave Emission Model of Layered Snowpacks to Coarse-Grained Snow", *Remote Sensing of Environment*, 70(3), 317-325.

Mätzler C. (1998). Improved Born Approximation for scattering of radiation in a granular medium, *J. Appl. Phys.*, 83(11), 6111-6117.

Mätzler, C. (1994). Passive microwave signatures of landscapes in winter. *Meteorology Atmospheric Physics*, 54, 241−260.

Mätzler, C. (1997). "Autocorrelation functions of granular media with free arrangement of spheres, spherical shells or ellipsoids", *J. Applied Physics*, 81(3), 1509-1517.

Mesinger, F., Dimego, G., Kalnay, E., Mitchell, K., Shafran, P. C., Ebisuzaki, W., et al. (2006). North American regional reanalysis. *Bull. of the American Meteorol. Soc.*, 87(3), 343–360.

Montpetit B., A. Royer, J.-P. Wigneron, A. Chanzy and A. Mialon (2015a). Evaluation of multi-frequency bare soil microwave reflectivity models. *Remote Sensing of Enviro.*, 162, 186 - 195.

Montpetit B., A. Royer, A. Roy and A. Langlois (2015b). In-situ passive microwave parameterization of sub-arctic frozen organic soils. *IEEE Geoscience and Remote Sensing Letters*, Submitted.

Montpetit B., Royer A., Langlois A., Cliche P., Roy A., Champollion N., Picard G., Domine F., Obbard R. (2012). New short wave infrared albedo measurements for snow specific surface area retrieval, *Journal of Glaciology*, 58(211), doi: 10.3189/2012JoG11j248.

Montpetit, B., Royer, A., Roy, A., Langlois, A. and Derksen, C. (2013). Snow microwave emission modeling of ice lenses within a snowpack using the Microwave Emission Model for Layered Snowpacks, *IEEE Trans. on Geoscience and Remote Sensing*, 51(9), 4705- 4717.

Pan J., Durand M., Sandells M., Lemmetyinen J., Kim E.J., Pulliainen J., Kontu A. and C. Derksen (2016). "Differences Between the HUT Snow Emission Model and MEMLS and Their Effects on Brightness Temperature Simulation," *IEEE Transactions on Geoscience and Remote Sensing*, 54(4), 2001-2019, doi: 10.1109/TGRS.2015.2493505

Picard, G., Brucker, L., Roy, A., Dupont, F., Fily, M., Royer, A., and Harlow, C. (2013). Simulation of the microwave emission of multi-layered snowpacks using the Dense Media Radiative transfer theory: the DMRT-MLmodel, *Geosci. Model Dev.*, 6, 1061–1078, doi:10.5194/gmd-6-1061-2013.

Picard, G., Royer, A., Arnaud, L., and Fily, M. (2014). Influence of meter-scale wind-formed features on the variability of the microwave brightness temperature around Dome C in Antarctica, *The Cryosphere*, 8, 1105–1119, doi:10.5194/tc-8-1105-2014.

Proksch M., C. Mätzler, A. Wiesmann, J. Lemmetyinen, M. Schwank, H. Löwe and M. Schneeball (2016). MEMLS3&a: Microwave Emission Model of Layered Snowpacks adapted to include backscattering.Geosci. Model Dev. Discuss., 8, 1–48, 2015 www.geosci-model-dev-discuss.net/8/1/2015/ doi:10.5194/gmdd-8-1-2015

Proksch, M., Löwe, H., and Schneebeli, M (2015). Density, specific surface area, and correlation length of snow measured by high-resolution penetrometry, *J. Geophys. Res. Earth Surf.,* 120, 346–362, doi:10.1002/2014JF003266.

Pulliainen J.T., J. Grandell, and M. T. Hallikainen (1999). “HUT snow emission model and its applicability to snow water equivalent retrieval,” *IEEE Trans. Geosci. Remote Sens.*, 37(3), 1378–1390.

Riche F., M Schneebeli and SA Tschanz (2012). Design-based stereology to quantify structural properties of artificial and natural snow using thin sections. *Cold regions science and*

technology 79, 67-74.

Roy A., A. Royer, O. St-Jean-Rondeau, B. Montpetit, G. Picard, A. Mavrovic, N. Marchand, and A. Langlois (2016). Microwave snow emission modeling uncertainties in boreal and subarctic environments, *The Cryosphere*, 10, 623-638, doi:10.5194/tc-10-623-2016.

Roy V., K. Goita, A. Royer, A. E. Walker, and B. E. Goodison (2004). "Snow water equivalent retrieval in a Canadian boreal environment from microwave measurements using the HUT snow emission model," *IEEE Trans.s on Geoscience and Remote Sensing*, 42(9), 1850–1859.

Roy, A., Picard, G., Royer, A., Montpetit, B., Dupont, F., Langlois, A., Derksen, C., and Champollion, N. (2013). Brightness Temperature Simulations of the Canadian Seasonal Snowpack Driven by Measurements of the Snow Specific Surface Area, *IEEE T. Geosci. Remote*, 51, 4692–4704, doi:10.1109/TGRS.2012.2235842.

Rutter, N., Essery, R., Pomeroy, J., Altimir, N., Andreadis, K., Baker, I., Barr, A., Bartlett, P., Boone, A., Deng, H., Douville, H., Dutra, E., Elder, K., Ellis, C., Feng, X., Gelfan, A., Goodbody, A., Gusev, Y., Gustafsson, D., Hellström, R., Hirabayashi, Y., Hirota, T., Jonas, T., Koren, V., Kuragina, A., Lettenmaier, D., Li, W.-P., Luce, C., Martin, E., Nasonova, O., Pumpanen, J., Pyles, R. D., Samuelsson, P., Sandells, M., Schädler, G., Shmakin, A., Smirnova, T. G., Stähli, M., Stöckli, R., Strasser, U., Su, H., Suzuki, K., Takata, K., Tanaka, K., Thompson, E., Vesala, T., Viterbo, P., Wiltshire, A., Xia, K., Xue, Y., and Yamazaki, T.: Evaluation of forest snow processes models (SnowMIP2), *J. of Geophysical Research: Atmospheres*, 114, doi:10.1029/2008JD011063.

Rutter N., Sandells, M., Derksen C., Toose P., Royer A., Montpetit B., Langlois A., Lemmetyinen J., and J. Pulliainen (2014). Snow stratigraphic heterogeneity within ground-based passive microwave radiometer footprints: Implications for emission modeling, *J. of Geophysical Research: Earth Surface*, 119, doi:10.1002/2013JF003017.

899 Sandells M., R. Essery, N. Rutter, L. Wake, L. Leppänen, and J.
900 Lemmetyinen (2016). Microstructure representation of snow in coupled snowpack and
901 microwave emission models. *The Cryosphere Discuss.*, doi:10.5194/tc-2016-181.
902 Schwank M., K. Rautiainen, C. Mätzler, M. Stähli, J. Lemmetyinen, J. Pulliainen, J. Vehviläinen,
903 A. Kontu, J. Ikonen, C. Bauduin-Ménard, M. Drusch, A. Wiesmann, and U. Wegmüller
904 (2014). Model for Microwave Emission of a Snow-Covered Ground with Focus on L Band,
905 *Remote Sens. Environ.*, 154, 180-191.
906 Shih, S.-E., Ding, K.-H., Kong, J. A., Yang, Y. E., Davis, R. E., Hardy, J. P., and Jordan, R.
907 (1997). Modeling of millimeter wave backscatter of time-varying snowcover, *Prog.*
908 *Electromagn. Res.*, 16, 305–330.
909 Tedesco M. and E. J. Kim (2006). "Intercomparison of Electromagnetic Models for Passive
910 Microwave Remote Sensing of Snow." *IEEE Transactions on Geoscience and Remote*
911 *Sensing*, 44(10), 2654–2666.
912 Tsang L., Ding K.-H, Huang S. and Xu X. (2013). Electromagnetic Computation in Scattering of
913 Electromagnetic Waves by Random Rough Surface and Dense Media in Microwave Remote
914 Sensing of Land Surfaces, Invited review paper, *Proc.s of the IEEE TGARS*, 101(2), 255-279.
915 Tsang, L. and Kong, J. A. (2001). *Scattering of electromagnetic waves*, 3, Advanced Topics,
916 Wiley Interscience.
917 Tsang, L., Pan, J., Liang, D., Li, Z., Cline, D. W., and Y. Tan (2007). Modeling active
918 microwave remote sensing of snow using dense media radiative transfer (DMRT) theory with
919 multiple- scattering effects, *IEEE Transactions on Geoscience and Remote Sensing*, 45, 990–
920 1004, doi:10.1109/TGRS.2006.888854.
921 Wegmüller U. and C. Mätzler (1999) "Rough bare soil reflectivity model," IEEE Trans. Geosci.
922 Remote Sens., 37, 3, 1391–1395.
923 Wiesmann A., and C. Mätzler (1999) "Microwave emission model of layered snowpacks",
924 *Remote Sensing of Environment*, 70(3), 307-316.

925 Wiesmann A., C. Mätzler and T. Weise (1998). "Radiometric and structural measurements of
926 snow samples", *Radio Sci.*. 33(2), 273-289.

927 **Table 1** Comparison between basics of DMRT-ML/-QMS, MEMLS and HUT-nlayers models. See below for the definitions of terms
928
929

Model	**DMRT-ML**		**DMRT-QMS**	**MEMLS (V3)**[1]		**HUT-nlayers**	
Version	V1.6 (with several options)		V 0.1	IBA version	Empirical version	2015	
Physical principle	Maxwell equations + several approximations considering a collection of densely packed sticky spheres			Empirical relationships between micro-structure and scatt/abso/ext coefficients and empirical relation for the dependence of the polarization factors on volume fraction			
Theory	Dense Media Radiative Transfer Model (Shih et al. 1997) (Tsang et al., 2013)			Improved Born Approxi-mation (IBA) [2] (Mätzler,1998)	Empirical scattering coef. (Weismann et al., 1998)	Semi-empirical relation	
Typical range of frequency	1 - 100 GHz						
Approxi-mations Options	Recommended option	Research option	Quasi-Crystalline Approximation (QCA) of Mie scattering	• Combination of coherent and incoherent (scattering) reflection between interface layers • Coherence effect for thin ice layer		• Empirical scat. coef. • Semi-empirical absorption coef.	
	• QCA-CP[3] • Rayleigh assumption • Optional correction for large particles (Grody, 2008) • Mono-disperse sphere radius • No stickiness	• QCA-CP • Rayleigh assumption • No large particles • Poly-disperse (i.e. Rayleigh distribution) • No stickiness		• IBA: option 12	• Different scattering coef.: options 8,10,11	$\kappa_e(1/\mathrm{m}) = \alpha f^2 D_{eff}^{2.8}$ [6]	$\kappa_e(1/\mathrm{m}) = \beta\left(f^4 D_{eff}^6\right)^{0.2}$ [7]
	• Optional stickiness • Optional bubbly ice		• Optional stickiness	• Ice without air bubble (p_{ex}=0)		• Ice as high density snow with R_{eff}=0	

Model	DMRT-ML	DMRT-QMS	MEMLS (V3)[1]	HUT-nlayers
Snow micro-structure parametri-zation[4]	Spheres defined by their radius (Ro) and their stickiness (τ)		Correlation length (p_c or p_{ex}) For 5 to 100 GHz, the model is defined by the correlation length range from 0.05 up to 0.6 mm (Mätzler and Wiesmann, 1999)	Grain geometrical extent (D_{max}) Grain effective diameter ($D_{max,eff}$)
Liquid Water content	Wetness fractional volume of water with respect to ice vol.	No	Volumetric liquid water content W: 0 to about 0.15	Snow moisture (up to several %)
Radiative transfer between layers	DISORT[5] (recommended 64 streams or more)	DISORT[5] by eigenvalue-quadrature analysis	2 or 6 streams	1 streams (Empirical coef. for forward scatt q=0.96)
	Fresnel reflection coef. for snow/snow and snow/atmosphere interfaces			
Main Ref.	Picard et al., 2013 Brucker et al., 2011 Roy et al., 2013 Dupont et al., 2014	Chang et al., 2014 Huang et al., 2012 Liang et al., 2008 Tsang et al., 2007	Proksch et al., 2016 Mätzler and Wiesmann (2014) Wiesmann and Mätzler, 1999 Mätzler and Wiesmann, 1999 Wiesmann et al., 1998 Mätzler 1996, 97, 98, 2004 Schwank et al., 2015	Lemmetyinen et al., 2010a Pulliainen et al., 1999 Kontu and Pulliainen, 2010
Web Site	Open source GPL license http://lgge.osug.fr/~picard/dmrtml/	http://web.eecs.umich.edu/~leutsang/Available%20Resources.html	http://www.iapmw.unibe.ch/research/projects/snowtools/memls.html	Upon request

930

931 [1] MEMLS Version 3 (2014) uses updated formulas for the dielectric constants of ice and water. An L-band version of MEMLS was used by

932 Schwank et al. (2015), assuming a simplified one-layer snowpack.

933 [2] IBA: the Improved Born Approximation (IBA) (Mätzler, 1998) expresses the scattering coefficient in terms of the Fourier transform of the

934 two-point correlation function.

935 [3] QCA: The quasi-crystalline approximation (QCA) consists of approximating the resolution of the multiple scattering calculation in a dense
936 porous environment by regarding this medium as a roughly crystalline structure, implying assumptions on the position of two particles
937 between them considered fixed.
938 QCA-CP: QCA can be optionally improved by the so-called Coherent Potential (QCA-CP) (Tsang and Kong, 2001). The basic concept of the
939 CP is to regard the medium near each scatterer as an effective medium with a uniform effective scattering function of aggregates, which
940 implies that the function remains constant in space. The CP approximation thus makes it possible to solve the calculation of the coherent
941 potential Green's operator for multiple scattering (and in the QCA context in our case) assumed as constant in space.
942 [4] See text for the snow microstructure parameterization of each model.
943 [5] The Discrete Ordinate Method (DISORT) is used to numerically solve the radiative transfer equation (Jin, 1994)
944 [6] Extinction coefficient κ_e: $\alpha = 0.000415$, relationship for 18-60 GHz, Hallikainen et al. (1987)
945 [7] Extinction coefficient κ_e : $\beta = 0.461$ Roy et al. (2004)
946
947